Computers and Geotechnics 132 (2021) 103971

Contents lists available at ScienceDirect

Computers and Geotechnics

journal homepage: www.elsevier.com/locate/compgeo

Research Paper

A fully coupled hydromechanical XFEM model for the simulation of 3D non-planar fluid-driven fracture propagation

Fang Shi [a,*], Jishan Liu [b]

[a] Jiangsu Key Laboratory of Advanced Manufacturing Technology, Huaiyin Institute of Technology, Huai'an, Jiangsu 223003, China
[b] Department of Chemical Engineering, School of Engineering, The University of Western Australia, 35 Stirling Highway, Perth, WA 6009, Australia

ARTICLE INFO

Keywords:
XFEM
3D hydraulic fracturing
Non-planar fracture
Reduction technique
Shale gas reservoir

ABSTRACT

Field data suggest that hydraulic fractures under in situ conditions are three-dimensional and non-planar in shale gas reservoirs. In this study, a fully coupled deformation, fracture growth, and fluid flow model is developed to simulate this complex phenomenon with a focus on the reduction of the total computational effort. An extended finite element method with high-order tip enrichment functions is used to simulate the rock deformation while the finite element method for the laminar flow in fractures. The explicit fracture representation is adopted to describe the non-planar 3D fractures. Schemes for identifying the fluid elements, selecting the enriched nodes, and subdividing the enriched elements are presented. The Newton-Raphson scheme is used to solve the coupled equilibrium and fluid flow equations in an element-by-element fashion. Within each Newton-Raphson iteration step, only enriched degrees of freedom are involved in the solution process by using the reduction technique to further reduce the computational effort. A displacement extrapolation method considering high-order terms is proposed to extract stress intensity factors from the displacement field. Several examples are performed to demonstrate the applicability and effectiveness of the proposed approach. The effectiveness of MPI parallel implementation of the proposed method is also investigated.

1. Introduction

In the shale gas exploitation area (Economides and Martin, 2007), hydraulic fracturing has been widely applied to improve the productivity of hydrocarbons by pumping high-pressure fluid into the reservoirs to artificially create flow paths consisted of hydraulic fractures. There are many other applications of hydraulic fracturing, such as underground disposal or storage of waste (Raziperchikolaee et al., 2013), extraction of geothermal energy (Kumari et al., 2018), preconditioning in cave mining (He et al., 2016), measurement of in-situ stress (Hayashi et al., 1997), etc. In order to gain a better understanding of these complex phenomena, it's of great necessity to construct reliable numerical models to investigate the mechanism of hydraulic fracturing.

In recent decades, some theoretical hydraulic fracturing models (Adachi et al., 2007) available for simple geometric configurations have been derived, such as the well-known PKN model for long fractures of small height (Perkins and Kern, 1961; Nordgren, 1972), the KGD model (Klerk, 1969) for short fractures, and the penny-shaped model for radial fractures (Sneddon, 1946). In recent years, on account of improvements in computer technology, various numerical methods (Adachi et al., 2007; Gupta and Duarte, 2014) were proposed and applied to study the hydraulic fracturing mechanism in which some key mechanical processes such as the deformation of rock matrix, the growth of hydraulic fractures, and the fluid flow within fractures have to be carefully addressed. Among these methods, the most frequently used include the finite element method (FEM) (Bao et al., 2014), the distinct element method (Shimizu et al., 2011), and the displacement discontinuity method (DDM) (Tang et al., 2019), etc. The FEM was early applied (Papanastasiou, 1999) in hydraulic fracturing simulation and shows great flexibility when the number of fractures is small. However, when it comes to complex or 3D non-planar geometric configuration, the FEM shows less efficiency due to the remeshing of the propagated fractures and the induced data mapping between meshes with different mesh structures. Seeing the shortcomings of the conventional FEM, some effective improvement measures have been put forward, such as the extended finite element method (XFEM) (Belytschko and Black, 1999; Moës et al., 1999) in which enrichment functions and additional enriched nodes are introduced to describe the discontinuous displacement field around fractures.

The XFEM is proposed under the framework of the partition of unity

* Corresponding author.
E-mail address: shifang@hyit.edu.cn (F. Shi).

https://doi.org/10.1016/j.compgeo.2020.103971
Received 4 August 2020; Received in revised form 27 November 2020; Accepted 9 December 2020

theory (Melenk and Babuška, 1996) and shows exceptional promise for applications to hydraulic fracturing simulation due to the significant advantages of its mesh-independent feature. Early studies on applications of the XFEM to hydraulic fracturing simulation have been carried out by Lecampion (2009), Dahi-Taleghani and Olson (2011), Gordeliy and Peirce (2013), et al. A recent review of the literature on the applications of the XFEM to fluid-driven fractures can be found in our previous work (Shi et al., 2016; Shi et al., 2017). Field data of hydraulic fracturing in shale gas formation suggests that hydraulic fractures in real conditions are complex, 3D, and non-planar (Adachi et al., 2007). Nevertheless, 3D XFEM-based models were seldom reported in the published studies. Gupta and Duarte (2018) established a tightly-coupled numerical model for 3D non-planar hydraulic fracturing simulation in the framework of the generalized finite element method (GFEM). Haddad and Sepehrnoori (2016) developed an XFEM-based cohesive zone model (CZM) for 3D multiple-cluster hydraulic fracturing simulation using commercial software Abaqus. Paul et al. (2018) established an XFEM-based CZM model to simulate 3D non-planar fluid-driven fracture propagation in the porous rock matrix. Among the few XFEM-based models, the fracture tip enrichments are neglected due to the difficulties in its 3D implementation, resulting in reduced approximation quality and other significant drawbacks. Firstly, the fractures must propagate completely through at least one element (Haddad and Sepehrnoori, 2016), and the fracture front must coincide with the element edges rather than lie within elements (Haddad and Sepehrnoori, 2016). Secondly, owing to the lack of tip enrichment, the mesh needs to be highly refined around the propagated fracture front (Haddad and Sepehrnoori, 2016; Paul et al., 2018), causing the growth of the computational complexity.

In this study, we construct a fully coupled XFEM-based model for hydraulic fracturing simulation of 3D non-planar fractures. The model simultaneously accounts for the elastic deformation of the rock formation, the growth of fluid-driven fractures, and the laminar flow within fractures. Obviously, the total computational expenses increase dramatically for 3D problems compared to two-dimensional (2D) since the multiplication of element number as well as the degrees of freedoms (DOFs) number (from 2 to 3) of each node. Even with today's powerful computational facilities, it is still a challenging task to solve such large-scale coupled systems. To make the XFEM-based model suitable and effective for 3D field-scale simulation, the focus of this study is on the reduction of the computational effort and improvement of the robustness without losing numerical precision. For this purpose, we represent the fracture surface in an explicit way (Section 3.1), rather than the implicit methods. That is because implicit methods, such as the level set method (Duflot, 2007), can be computationally expensive owing to the solution of 3D hyperbolic equations (Bordas and Moran, 2006) required for level set updating, and may cause the concealment of the sharp features of 3D crack surfaces (Gupta and Duarte, 2014). Besides, high-order tip enrichment functions (Section 2.3) extracted from the Williams analytical solution (Williams, 1957) are used to improve the simulation accuracy of the displacement fields. A displacement extrapolation method considering high-order terms is proposed to extract stress intensity factors (SIFs) from the displacement field (Section 2.7). In the meantime, to overcome the difficulty in the implementation of fracture tip enrichment in the linear elastic fracture mechanics (LEFM) framework, we present several schemes to identify the fluid elements (Section 3.2), determine the enriched nodes (Section 3.3), partition the enriched elements for precise integration (Section 3.4). In order to further reduce the computational cost, the reduction technique (Section 2.6) is proposed to avoid the traditional DOFs during the solution process.

It should be pointed out that the permeability of the rock and fluid leak-off from the hydraulic fracture into the rock formation have not been considered in this study. Hence, the proposed model is inapplicable to simulate fluid-driven fractures in porous rock formations with high permeability or fractured formations with low permeability (Meng et al., 1996; Guo and Cheng, 2013). On the other hand, the stepwise fracture growth and ensuing pressure oscillations have been widely observed in the oil and gas industry (Okland et al., 2002), laboratory experiments (Lhomme et al., 2002; Trimonova et al., 2017; Peruzzo et al., 2019), and numerical simulations (Feng and Gray, 2017; Cao et al., 2018; Shovkun and Espinoza, 2019; Milanese et al., 2016; Secchi and Schrefler, 2014). It's believed that the fluid flow in the bulk media and the fluid exchange between the fracture and the surrounding (leak-off) are necessary for a numerical model to capture the phenomenon of stepwise fracture growth and fluid pressure oscillations. Pizzocolo et al. (2013) suggested a consolidation process around the crack tip as an explanation for the stepwise propagation phenomenon of a crack in a porous medium. Milanese et al. (2016) gave an explanation of the step-wise phenomenon based on Biot's theory. Feng and Gray (2017) showed that the rock permeability has a predominant influence on the step-wise pressure oscillations phenomenon, and the intensity of the pressure oscillations decreases with decreasing rock permeability (see Fig. 12 in their work for details). However, the stepwise fracture growth and ensuing pressure oscillations have not been captured in this study due to the assumption of impermeable rock formation; thus, the obtained results are smooth and continuous rather than in a stepwise and oscillating manner in this paper.

The following sections of this paper are organized as follows. Firstly, the theoretical framework of the XFEM-based model is briefly presented in Section 2. Section 3 is dedicated to discuss and solve the challenges in implementing the proposed 3D XFEM-based approach. Finally, several examples will be presented in Section 4 to demonstrate the applicability and effectiveness of the proposed approach. The effectiveness of MPI parallel implementation of the proposed method will be investigated in Section 4.7.

2. Problem formulation

Consider a fracture Γ_c within a domain Ω, as illustrated in Fig. 1. The pressure of the Newtonian and incompressible fluid inside the fracture is denoted by p. We impose stress $\mathbf{t}$ on boundary Γ_t and displacement $\bar{\mathbf{u}}$ on boundary Γ_u. $\mathbf{n}_{\Gamma_c}$ is the normal vector of Γ_c. The fluid is pumped into the fracture at a rate of Q. In addition, some assumptions are made as follows. The lag between the fluid front and the fracture front is not considered. Besides, it is supposed that the rock formation behaves as linear elastic and the fracture growth process is quasi-static.

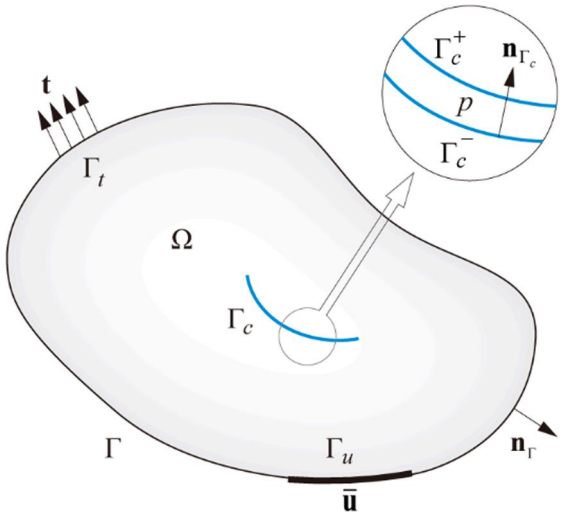

Fig. 1. Schematic of fluid-driven propagation within a domain Ω.

2.1. Deformation of the rock formation

The equilibrium equation of the quasi-static problem within the domain Ω can be written as

$$\nabla\cdot\boldsymbol{\sigma} = \mathbf{0} \tag{1}$$

along with the following boundary conditions

$$\begin{cases} \mathbf{u} = \bar{\mathbf{u}} & \text{on} \quad \Gamma_u \\ \boldsymbol{\sigma}\cdot\mathbf{n} = \mathbf{t} & \text{on} \quad \Gamma_t \\ \boldsymbol{\sigma}\cdot\mathbf{n}_{\Gamma_c} = p\mathbf{n}_{\Gamma_c} & \text{on} \quad \Gamma_c \end{cases} \tag{2}$$

where $\boldsymbol{\sigma}$ stands for the Cauchy stress tensor. The deformation of the rock matrix follows a linear relationship

$$\boldsymbol{\sigma} = \mathbf{D} : \boldsymbol{\varepsilon} \tag{3}$$

where $\mathbf{D}$ and $\boldsymbol{\varepsilon}$ represent the elasticity matrix of moduli and strain tensor, respectively.

2.2. Fluid flow

In this paper, the flow velocity in the direction normal to the fracture is neglected because of the extremely low permeability of the shale formation. Therefore, the flow can be treated as a 2D laminar flow problem which can be described by the mass conservation law in conjunction with Poiseuille's cubic law (Adachi et al., 2007). For each fluid element, as depicted in Fig. 2, we define a local coordinate system at the element center with two base vectors $\{\bar{\mathbf{e}}_1, \bar{\mathbf{e}}_2\}$ that satisfy the condition $\bar{\mathbf{e}}_1 \times \bar{\mathbf{e}}_2 = \mathbf{n}_{\Gamma_c}$. Then, for any point $\bar{\mathbf{x}} = \left(\bar{x}_1, \bar{x}_2\right)$ defined in the local coordinate system on the fluid-driven fractures, the strong form of the flow equation can be expressed as (Batchelor, 1967)

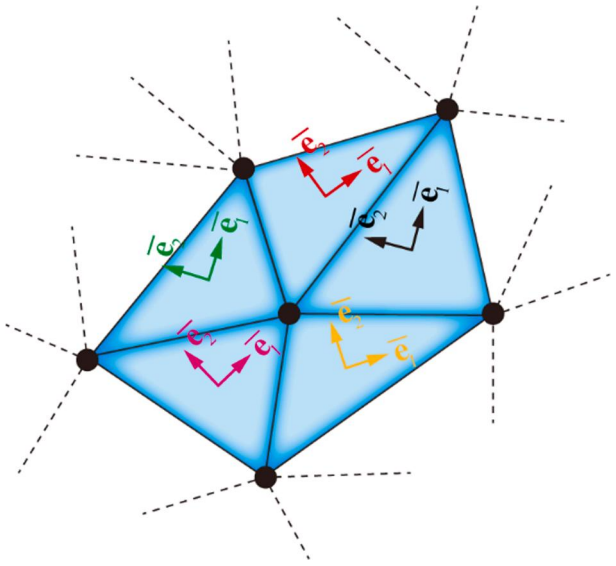

Fig. 2. Local coordinate system whose origin is positioned at the center of each fluid element colored in blue. The black dots represent fluid nodes. The base vector $\bar{\mathbf{e}}_1$ coincides with the vector from the center to the first node of a fluid element.

$$\frac{\partial w}{\partial t} - \nabla_{\bar{\mathbf{x}}}\left(\frac{w^3}{12\mu}\nabla_{\bar{\mathbf{x}}}p\right) = Q \tag{4}$$

where w is the fracture aperture, μ is the fluid viscosity, t is time, and $\nabla_{\bar{\mathbf{x}}}$ is a 2D gradient operator defined in the fracture plane Γ_c:

$$\nabla_{\bar{\mathbf{x}}} = \frac{\partial}{\partial \bar{x}_1}\bar{\mathbf{e}}_1 + \frac{\partial}{\partial \bar{x}_2}\bar{\mathbf{e}}_2 \tag{5}$$

2.3. The XFEM enrichment scheme

In the literature, researchers have proposed a variety of numerical methods for the simulation of fluid-driven fracture propagation process. The first family of methods is based on LEFM. The second family of methods based on the cohesive zone models is suitable for ductile formations or high-permeability formations (Wang, 2016), but usually requires very fine meshes to accurately capture the fracture process zone (Lecampion et al., 2018). Besides, although cohesive zone models have the ability to simulate mode I/II fracture growth, they are usually not able to simulate mixed-mode I/II/III fracture growth (Lecampion et al., 2018) which is very important for 3D hydraulic fracturing simulation as will be shown in this paper. Therefore, under the assumption (i.e., impermeable and brittle formation) made in this paper, the XFEM model based on LEFM is used to describe the displacement field around the fracture front.

For a fluid-filled fracture tip, Gordeliy and Peirce (2013) considered that the power-law exponent λ for the tip enrichment should satisfy $1/2 < \lambda < 1$. Besides, Klimenko and Taleghani (2018) suggested that λ might change from 1/2 to 2/3 as the hydraulic fracture changes from the toughness-dominated regime to the viscosity-dominated regime. As an alternative, besides the Heaviside enrichment function, tip enrichment functions with non-singular terms in addition to singular terms ($r^{1/2}$) are considered to account for the features of the displacement field around the fluid-filled fracture tip in this paper. This enrichment strategy in combination with the proposed 3D implementation scheme (Section 3) gives the ability to deal with hydraulic fracturing simulation problems without resorting to extremely fine meshes, which will be demonstrated in Section 4. For any point $\mathbf{x}$ in the domain Ω, its displacement $\mathbf{u}$ can be written as

$$\mathbf{u}(\mathbf{x}) = \sum_{I\in S_{all}} N_I^u(\mathbf{x})\mathbf{u}_I + \sum_{I\in S_{frac}} N_I^u(\mathbf{x})H(\mathbf{x})\mathbf{a}_I + \sum_{I\in S_{tip}} N_I^u(\mathbf{x})\sum_{l=1}^{10} F_l(\mathbf{x})\mathbf{b}_I^l \tag{6}$$

where S_{all}, S_{frac}, and S_{tip} are node sets of common nodes, Heaviside enriched nodes, and tip enriched nodes, respectively. $\mathbf{u}_I$, $\mathbf{a}_I$, and $\mathbf{b}_I^l (l = 1, 10)$ are displacement vectors of DOFs of nodes belonging to S_{all}, S_{frac}, and S_{tip}, respectively. N_I^u denotes the standard finite element shape function. Besides, the Heaviside enrichment function $H(\mathbf{x})$ takes the following form

$$H(\mathbf{x}) = \begin{cases} 1, & \text{if} \quad (\mathbf{x}-\mathbf{x}^*)\cdot\mathbf{n}_{\Gamma_c} \geqslant 0 \\ -1, & \text{otherwise} \end{cases} \tag{7}$$

in which $\mathbf{x}^*$ is the closest point on the fracture to point $\mathbf{x}$. Tip enrichment functions $F(\mathbf{x})$ for different orders of r, i.e., $\sqrt{r}$, r, and $r^{3/2}$ can be written as, respectively (Williams, 1957; Lan et al., 2013; Song et al., 2015):

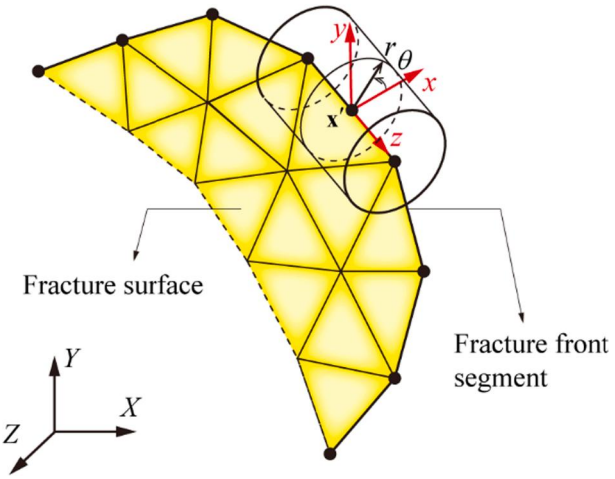

Fig. 3. Local Cartesian coordinate system (x, y, z) and local cylindrical coordinate system (r, θ, z) defined at the midpoint of the fracture front segment. The y-axis coincides with $\mathbf{n}_{\Gamma_c}$. The z-axis is defined along the direction of the fracture front segment.

$$\{F_l(r,\theta)\}_{l=1,\ldots,4} = \left\{\sqrt{r}\sin\frac{\theta}{2}, \sqrt{r}\cos\frac{\theta}{2}, \sqrt{r}\sin\theta\sin\frac{\theta}{2}, \sqrt{r}\sin\theta\cos\frac{\theta}{2}\right\} \tag{8}$$

$$\{F_l(r,\theta)\}_{l=5,6} = \{r\cos\theta, r\sin\theta\} \tag{9}$$

$$\{F_l(r,\theta)\}_{l=7,\ldots,10} = \left\{r^{3/2}\cos\frac{\theta}{2}, r^{3/2}\sin\frac{\theta}{2}, r^{3/2}\sin\theta\sin\frac{\theta}{2}, r^{3/2}\sin\theta\cos\frac{\theta}{2}\right\} \tag{10}$$

where r and θ are components of the local cylindrical coordinate system (r, θ, z) defined in the x-y plane of the local Cartesian coordinate system (x, y, z) originating from point $\mathbf{x}'$ which is the midpoint of each fracture front segment, as depicted in Fig. 3. The coordinates of point $\mathbf{x}$ in the local Cartesian coordinate system can be obtained as

$$\begin{Bmatrix} x \\ y \\ z \end{Bmatrix} = \mathbf{T}(\mathbf{x} - \mathbf{x}') \tag{11}$$

where $\mathbf{T}$ is the transformation matrix from the global Cartesian coordinate system (X, Y, Z) to (x, y, z).

2.4. Weak form of governing equations

By introducing the test function $\delta\mathbf{u}(\mathbf{x}, t)$, we can derive the weak form of the equilibrium equation

$$\int_\Omega \delta\boldsymbol{\varepsilon} : \boldsymbol{\sigma} d\Omega + \int_{\Gamma_c} [[\delta\mathbf{u}]] \cdot p\mathbf{n}_{\Gamma_c} d\Gamma = \int_{\Gamma_t} \delta\mathbf{u}\cdot\mathbf{t} d\Gamma \tag{12}$$

in which $[[\delta\mathbf{u}]] = \delta\mathbf{u}(\Gamma_c^+) - \delta\mathbf{u}(\Gamma_c^-)$ is the displacement jump across Γ_c. Assuming a zero flux along the fracture front (Kumar and Ghassemi, 2016), we introduce the test function $\delta p(\bar{\mathbf{x}}, t)$ into the fluid flow equation (Eq. (4)), then the weak form can be obtained after integrating by parts

$$\int_{\Gamma_c} \left(\delta p \frac{\partial w}{\partial t} - \frac{w^3}{12\mu}\nabla_{\bar{\mathbf{x}}}\delta p \cdot \nabla_{\bar{\mathbf{x}}} p - \delta p Q\right) d\Gamma = 0 \tag{13}$$

2.5. Discretization of governing equations

Substitute Eqs. (3) and (6) into Eq. (12), the discrete form of the equilibrium equation can be written as (Shi et al., 2017):

$$\mathbf{KU} - \mathbf{QP} - \mathbf{F}^{\text{ext}} = \mathbf{0} \tag{14}$$

in which $\mathbf{U}$ stands for the global displacement vector, $\mathbf{P}$ is the fluid pressure vector, $\mathbf{F}^{\text{ext}}$ is the force vector, and $\mathbf{Q}$ is the coupling matrix which transforms $\mathbf{P}$ to nodal forces:

$$\mathbf{Q} = \int_{\Gamma_c} (\mathbf{N}^w)^T \mathbf{n}_{\Gamma_c} \mathbf{N}^p d\Gamma \tag{15}$$

In Eq. (15), $\mathbf{N}^w$ denotes the shape function matrix which transfers the global displacement vector $\mathbf{U}$ to fracture aperture vector $\mathbf{w}$. In Eq. (14), the global stiffness matrix $\mathbf{K}$ can be assembled according to the following expression

$$\mathbf{K} = \begin{bmatrix} \int_\Omega (\mathbf{B}^{std})^T \mathbf{D}\mathbf{B}^{std} d\Omega & \int_\Omega (\mathbf{B}^{std})^T \mathbf{D}\mathbf{B}^{enr} d\Omega \\ \int_\Omega (\mathbf{B}^{enr})^T \mathbf{D}\mathbf{B}^{std} d\Omega & \int_\Omega (\mathbf{B}^{enr})^T \mathbf{D}\mathbf{B}^{enr} d\Omega \end{bmatrix} = \begin{bmatrix} \mathbf{K}_{ss} & \mathbf{K}_{se} \\ \mathbf{K}_{es} & \mathbf{K}_{ee} \end{bmatrix} \tag{16}$$

The linear hexahedral element with eight corner nodes is applied to mesh the model and construct the global stiffness matrix $\mathbf{K}$. For elements without enriched nodes, $2 \times 2 \times 2$ Gauss points are utilized to perform the integration. For elements that contain enriched nodes but no fracture surface, $6 \times 6 \times 6$ Gauss points are adopted. For elements that contain fracture surface, acceptable integration accuracy can be reached if enough number of Gauss points are adopted (Sukumar et al., 2000). Nonetheless, it might be quite possible that no Gauss point exists on one side of the fracture within the brick element, resulting in singularity of the stiffness matrix and loss of integration robustness. Therefore, with the purpose of improving robustness, accuracy, as well as convergence rate, the enriched elements which are completely or partially divided by the fracture should be divided into tetrahedrons (Loehnert et al., 2011). Details on the construction of tetrahedrons will be presented in Section 3.4.

Triangle elements with three nodes are used to discretize the fluid flow equation (Eq. (13)), thus the fluid pressure at point $\bar{\mathbf{x}}$ can be interpolated from nodal values p_I according to

$$p(\bar{\mathbf{x}}) = \sum_{I \in S_{fluid}} N_I^p(\bar{\mathbf{x}}) p_I \tag{17}$$

where N_I^p is the conventional finite element shape function of fluid elements, and S_{fluid} represents the set of fluid nodes.

Substitute Eq. (17) into Eq. (13), the discrete form of the fluid flow equation can be described by (Shi et al., 2017)

$$\mathbf{Q}^T\dot{\mathbf{U}} + \mathbf{HP} + \mathbf{S} = \mathbf{0} \tag{18}$$

where matrix $\mathbf{H}$ and vector $\mathbf{S}$ are the flow matrix and the source term, respectively

$$\mathbf{H} = \int_{\Gamma_c} \frac{w^3}{12\mu} (\nabla_{\bar{\mathbf{x}}}^T \mathbf{N}^p)(\nabla_{\bar{\mathbf{x}}} \mathbf{N}^p) d\Gamma \tag{19}$$

$$\mathbf{S} = \int_{\Gamma_c} (\nabla_{\bar{\mathbf{x}}} \mathbf{N}^p)^T Q d\Gamma \tag{20}$$

Time discretization of the governing equation (Eq. (18)) is performed using the implicit backward Euler scheme and details can be found in our recent paper (Shi et al., 2017). Within each time step, the coupled non-linear system equations are iteratively solved using the Newton-Raphson scheme with a backtracking algorithm (Shi et al., 2017).

2.6. Solution of the coupled equations

In order to solve the coupled equations (Eqs. (14) and (18)) using the Newton-Raphson scheme, the residual vector $\mathbf{R}^i$ can be written as

$$\mathbf{R}^i = \begin{bmatrix} \mathbf{0} & \mathbf{0} \\ -\mathbf{Q}^T & \mathbf{0} \end{bmatrix} \begin{pmatrix} \Delta\mathbf{U} \\ \Delta\mathbf{P} \end{pmatrix}^i + \begin{bmatrix} \mathbf{K} & -\mathbf{Q} \\ \mathbf{0} & -\Delta t\mathbf{H}^i \end{bmatrix} \begin{pmatrix} \mathbf{U} \\ \mathbf{P} \end{pmatrix}^i - \begin{pmatrix} \mathbf{F}^{\text{ext}} \\ \Delta t\mathbf{S}^i \end{pmatrix}^i \tag{21}$$

where i denotes Newton-Raphson iteration step number. The corresponding Jacobin matrix takes the following form

$$\mathbf{J}^i = \begin{bmatrix} \mathbf{K} & -\mathbf{Q} \\ -\mathbf{Q}^T & -\Delta t\mathbf{H}^i \end{bmatrix} \tag{22}$$

Using the reduction technique proposed in our previous work (Shi et al., 2017), the reduced residual vector $\mathbf{R}_R^i$ and reduced Jacobin matrix $\mathbf{J}_R^i$ can be respectively written as

$$\mathbf{R}_R^i = \begin{bmatrix} \mathbf{0} & \mathbf{0} \\ -\mathbf{Q}_e^T & \mathbf{0} \end{bmatrix} \begin{pmatrix} \Delta\mathbf{U}_e \\ \Delta\mathbf{P} \end{pmatrix}^i + \begin{bmatrix} \mathbf{K}_{ee} - \mathbf{K}_{es}\mathbf{K}_{ss}^{-1}\mathbf{K}_{se} & -\mathbf{Q}_e \\ \mathbf{0} & -\Delta t\mathbf{H}^i \end{bmatrix} \begin{pmatrix} \mathbf{U}_e \\ \mathbf{P} \end{pmatrix}^i - \begin{pmatrix} -\mathbf{K}_{es}\mathbf{K}_{ss}^{-1}\mathbf{F}_s^{\text{ext}} \\ \Delta t\mathbf{S}^i \end{pmatrix}^i \tag{23}$$

$$\mathbf{J}_R^i = \begin{bmatrix} \mathbf{K}_{ee} - \mathbf{K}_{es}\mathbf{K}_{ss}^{-1}\mathbf{K}_{se} & -\mathbf{Q}_e \\ -\mathbf{Q}_e^T & -\Delta t\mathbf{H}^i \end{bmatrix} \tag{24}$$

where $\mathbf{Q}_e$ is obtained by removing terms related to the conventional DOFs from the coupling matrix $\mathbf{Q}$, $\mathbf{U}_e$ is the displacement vector of the enriched DOFs, $\mathbf{F}_s^{\text{ext}}$ is obtained by removing terms related to the enriched DOFs from the force vector $\mathbf{F}^{\text{ext}}$.

Therefore, the following equation can be obtained

$$\mathbf{J}_R^i \Delta\widehat{\mathbf{U}}^i = \mathbf{R}_R^i \tag{25}$$

where $\Delta\widehat{\mathbf{U}} = \begin{bmatrix} \Delta\mathbf{U}_e \\ \Delta\mathbf{P} \end{bmatrix}$. The resulting Eq. (25) is assembled and solved in an element-by-element fashion (Smith et al., 2014) without direct assembly of element matrices. Then, $\widehat{\mathbf{U}}^{i+1}$ can be updated according to $\widehat{\mathbf{U}}^{i+1} = \widehat{\mathbf{U}}^i - \Delta\widehat{\mathbf{U}}^i$ until the following criterion is satisfied:

$$\frac{\left\| \Delta\widehat{\mathbf{U}}^i - \Delta\widehat{\mathbf{U}}^{i-1} \right\|}{\left\| \Delta\widehat{\mathbf{U}}^{i-1} \right\|} \leqslant \varepsilon_{\text{tol}} \tag{26}$$

where ε_{tol} is taken as 10^{-6} in this study and $\|\|$ denotes L_2 norm operator. It should be noted that the reduction technique can also (Shi et al., 2017) be used to solve the linear system (Eq. (14)) without fluid pressure (Section 4.1) or with constant fluid pressure (Section 4.2).

2.7. Fracture growth model

During the hydraulic fracturing treatment, it is preferred that the hydraulic fracture initiates and propagates directly from the wellbore in the direction of the preferred in-situ stress orientation. In practice, however, the hydraulic fracture usually propagates in a mixed-mode I/II/III, which sometimes leads to curving and possibly segmentation of the fracture front. Segmented fractures caused by mixed-mode fracturing has been widely found both in nature (Rubin, 1995; Abelson and Agnon, 1997) and laboratory investigations (Wu et al., 2009; Bunger et al., 2017; Ketterij and Pater, 1999). Researchers (Wu et al., 2009) show that in quasi-brittle materials, even a small mode III component of stress intensity factors may cause fracture segmentation for a fluid-driven fracture. In this paper, the Schöllmann's criterion (Schöllmann et al., 2002) which is based on the assumption that the propagation occurs in the direction of maximum principal stress σ_1 ahead of the crack front is adopted as the crack propagation criterion. In this criterion, all fracture modes are considered making it well-suited for computational implementations aimed at fully 3-D crack growth prediction. Nonetheless, since the geometrical configuration of the segmented fracture is very complex (Wu et al., 2009; Bunger et al., 2017; Ketterij and Pater, 1999), it remains a challenging task to explicitly simulate the segmentation process from the perspective of numerical implementation, especially for a large-scale hydraulic fracturing simulation. As a compromise, the adopted Schöllmann's criterion assumes continuity of the fracture front, consequently causing the failure of the proposed model to predict the segmentation phenomenon of the fracture front.

Details of the Schöllmann's criterion can be found in Schöllmann et al. (2002). In accordance with this criterion, the fracture propagation direction is determined by two fracture deflection angles, i.e., the kinking angle θ_0 and the twisting angle ψ_0 as depicted in Fig. 4. The kinking angle θ_0 is determined by the rules:

$$\frac{\partial\sigma_1}{\partial\theta} = 0\Big|_{\theta=\theta_0}, \frac{\partial^2\sigma_1}{\partial\theta^2} < 0\Big|_{\theta=\theta_0} \tag{27}$$

where the maximum principal stress σ_1 is calculated on a virtually created cylindrical surface (Schöllmann et al., 2002) using the following equation

$$\sigma_1 = \frac{\sigma_\theta}{2} + \frac{1}{2}\sqrt{\sigma_\theta^2 + 4\tau_{\theta z}^2} \tag{28}$$

In Eq. (28), the stress components σ_θ and $\tau_{\theta z}$ can be expressed in terms of SIFs:

$$\sigma_\theta = \frac{K_{\text{I}}}{4\sqrt{2\pi r}}\left[3cos\left(\frac{\theta}{2}\right) + cos\left(\frac{3\theta}{2}\right)\right] - \frac{K_{\text{II}}}{4\sqrt{2\pi r}}\left[3sin\left(\frac{\theta}{2}\right) + 3sin\left(\frac{3\theta}{2}\right)\right] \tag{29}$$

$$\tau_{\theta z} = \frac{K_{\text{III}}}{\sqrt{2\pi r}}cos\left(\frac{\theta}{2}\right) \tag{30}$$

where r stands for the distance from the fracture front to the virtual cylindrical surface. In the present study, a golden section search algorithm (Press et al., 1992) is applied to find the kinking angle θ_0 which maximizes σ_1. Once determining the kinking angle θ_0, the twisting angle ψ_0 can be obtained by

$$\psi_0 = \frac{1}{2}arctan\left[\frac{2\tau_{\theta z}(\theta_0)}{\sigma_\theta(\theta_0)}\right] \tag{31}$$

For the fracture front vertex i, the magnitude of front advancement can be obtained by

$$\Delta a_i = \begin{cases} 0, & \text{if } K_{\text{I}eq} < K_{\text{I}c} \\ \Delta a_{max}\dfrac{\left(K_{\text{I}eq}^i - K_{\text{I}c}\right)}{K_{\text{I}eq}^{max} - K_{\text{I}c}}, & \text{if } K_{\text{I}eq} \geqslant K_{\text{I}c} \end{cases} \tag{32}$$

where Δa_{max} is the maximum fracture front advancement and taken as the average characteristic length l_c of enriched elements ($l_c = \overline{V}_{enrich}^{1/3}$, where $\overline{V}_{enrich}$ represents the average volume of all enriched elements);$K_{\text{I}eq}$ is the equivalent mode-I SIF and can be computed using the following expression (Schöllmann et al., 2002)

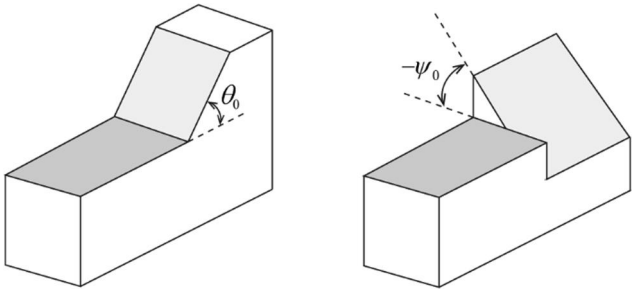

Fig. 4. Depiction of the kinking angle θ_0 and the twisting angle ψ_0 for 3D fracture propagation.

$$K_{1eq} = \frac{1}{2}cos\left(\frac{\theta_0}{2}\right)\left\{K_1 cos^2\left(\frac{\theta_0}{2}\right) - \frac{3}{2}K_{II}sin(\theta_0) + \sqrt{\left[K_1 cos^2\left(\frac{\theta_0}{2}\right) - \frac{3}{2}K_{II}sin(\theta_0)\right]^2 + 4K_{III}^2}\right\} \tag{33}$$

Besides, K_{Ic} is the mode-I fracture toughness. It should be noted that if the length of the newly created fracture front segment is larger than l_c, a new vertex should be added at the midpoint of segment.

Because of the assumption of the quasi-static fracture propagation, the maximum value of equivalent mode-I SIF, K_{leq}^{max}, at fracture front vertexes should equal the mode-I fracture toughness at each time step. For a given fracture propagation step, dynamic time step (Bao et al., 2014; Tang et al., 2019; Gupta and Duarte, 2018) Δt is used to fulfill the following condition

$$\left(1.0 - \varepsilon_{tol}^t\right)K_{Ic} \leqslant K_{leq}^{max} \leqslant \left(1.0 + \varepsilon_{tol}^t\right)K_{Ic} \tag{34}$$

where ε_{tol}^t is the tolerance and taken as 0.01 in this study.

Due to the non-uniform pressure distribution near the fracture front, the energy-based stress intensity factor extraction methods including the J-integral method as well as the interaction integral method (Gupta et al., 2017) are not chosen to calculate the SIFs. Instead, the displacement extrapolation method in which boundary conditions on fracture surfaces do not need to be specially considered is selected. Similar to the tip enrichment functions, high-order terms are used in the proposed displacement extrapolation method. For a mode-I crack, the vertical displacement on both sides of the fracture surface can be written as (Kanninen and Popelar, 1985)

$$v(r, \quad \pi) = K_I\frac{\kappa+1}{2G}\sqrt{\frac{r}{2\pi}} + Ar^{3/2} + Br^{5/2} + \mathscr{O}(r^{7/2}) \tag{35}$$

$$v(r, \quad -\pi) = -K_I\frac{\kappa+1}{2G}\sqrt{\frac{r}{2\pi}} - Ar^{3/2} - Br^{5/2} + \mathscr{O}(r^{7/2}) \tag{36}$$

where parameters A and B depend on material parameters, load conditions, and geometry configuration. G represents the shear modulus, and κ represents the Kolosov constant. Consequently, the vertical displacement jump can be written as

$$[[v(r)]] = K_I\frac{\kappa+1}{G}\sqrt{\frac{r}{2\pi}} + 2Ar^{3/2} + 2Br^{5/2} + \mathscr{O}(r^{7/2}) \tag{37}$$

Let's define $K_I^*(r) := \sqrt{\frac{2\pi}{r}}\frac{G}{\kappa+1}[[v(r)]]$, then we have

$$K_I^*(r) = K_I + \widetilde{A}r + \widetilde{B}r^2 + \mathscr{O}(r^3) \tag{38}$$

where parameters $\widetilde{A}$ and $\widetilde{B}$ are constants. Given three different radius, $r_a > r_b > r_c$, the mode-I SIF can be obtained according to

$$K_I = \frac{K_I^*(r_a)c_1 + K_I^*(r_b)c_2 + K_I^*(r_c)c_3}{c_1 + c_2 + c_3} \tag{39}$$

with

$$\begin{aligned} c_1 &= r_b r_c^2 - r_b^2 r_c \\ c_2 &= r_c r_a^2 - r_c^2 r_a \\ c_3 &= r_a r_b^2 - r_a^2 r_b \end{aligned} \tag{40}$$

Compared to the conventional displacement extrapolation method (Gupta et al., 2017; Guinea et al., 2000) where only two points behind the fracture front are selected to calculate SIFs, three points (points a, b, and c) are adopted in this proposed method, leading to improved accuracy (see Section 4.1.2 for details). In this paper, these three points are uniformly spaced at a distance of Δr, that is, $\Delta r = r_a - r_b = r_b - r_c$. The same procedure can be followed to extract K_{II} and K_{III} from the displacement field.

3. Computational methodology

3.1. Description of the fracture surfaces

Due to the expensive computational cost and the drawback of describing special fracture surface features such as kinking, twisting and branching (Gupta and Duarte, 2014), the implicit description method, such as the widely used level set method, is not employed in this paper. Instead, as shown in Fig. 5(a), the fracture surface Γ_c is explicitly represented (Baydoun and Fries, 2012) by a set of spatial triangle patches T_i, i.e., $\Gamma_c = \cup_{i=1}^{N_{\text{tri}}} T_i$, where N_{tri} is the total number of triangle patches. Each triangle patch T_i is composed of three triangle points T_i^1 to T_i^3 indexed in an anti-clockwise order. Given a set of triangle points in $\mathbf{R}^3$ which are related by a connectivity matrix, the explicit description method is able to select elements that need to be enriched in the FE mesh and determine fluid elements. After the propagation, the fracture surfaces are updated by adding new triangle patches around the fracture front, as shown in Fig. 5(b).

3.2. Identification of the fluid elements

First of all, as shown in Fig. 6(a), for an element entirely cut by a fracture (in other words, not intersected by the fracture front), the nodes of fluid elements can be directly determined by calculating the intersections of element edges and the fracture surface according to the segment/triangle intersection algorithm (Jiménez et al., 2010). In order

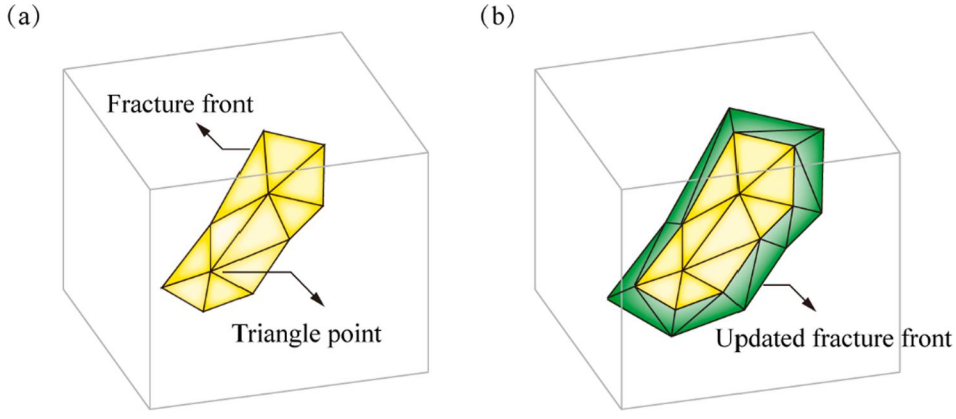

Fig. 5. Illustration of the fracture surface: (a) explicit description of the fracture composed of flat triangles and straight edges; (b) the updated fracture after propagation.

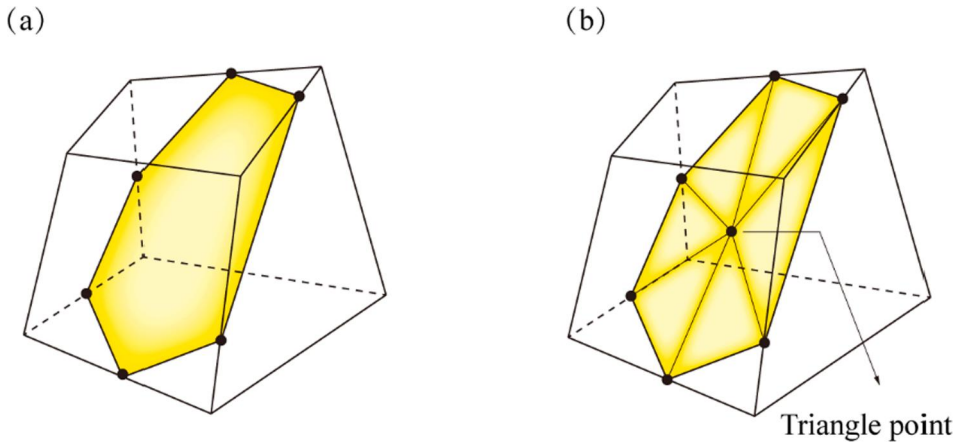

Fig. 6. Determination of fluid nodes: (a) no triangle point on the fracture surface; (b) one triangle point on the fracture surface.

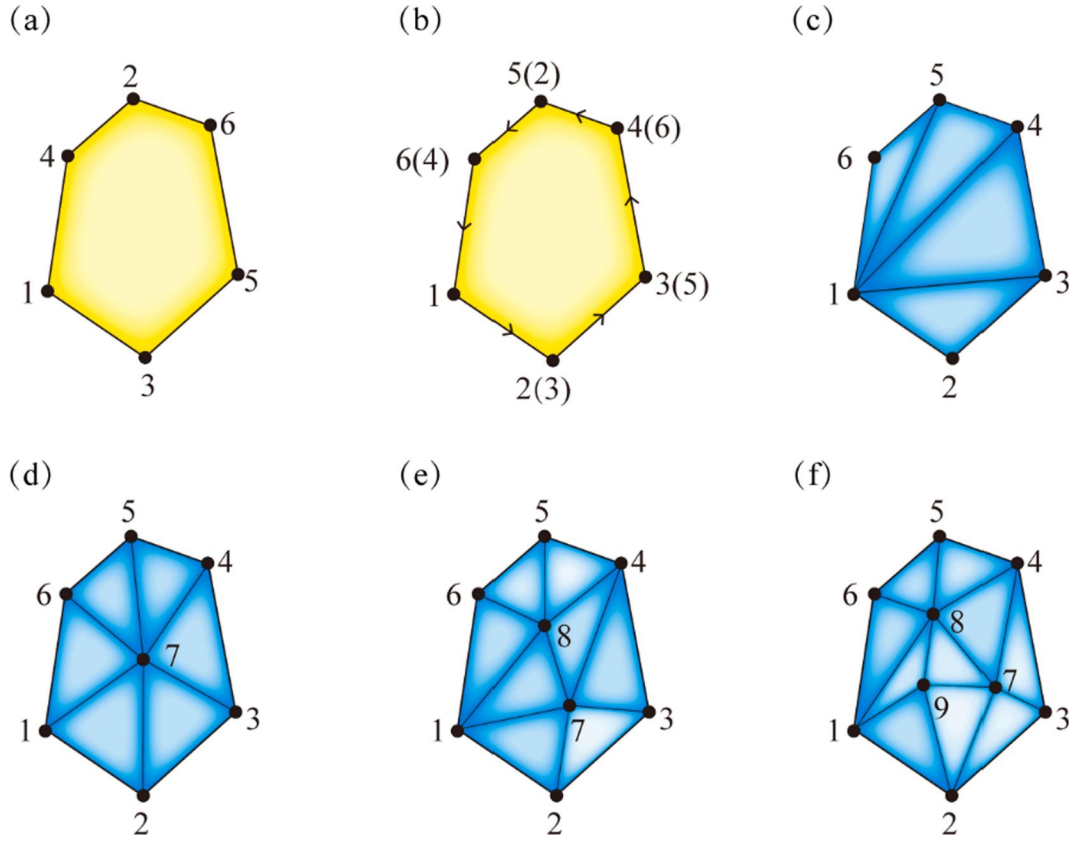

Fig. 7. Construction of fluid elements: (a) intersections of element edges and the fracture surface; (b) sorted fluid nodes in an anti-clockwise order; (c) generation rules for fluid elements when there is no triangle point on the crack surface; and generation rules for fluid elements when there are one (d), two (e), and three (f) triangle points on the crack surface. Black dots represent fluid nodes, yellow triangles represent the explicit fracture surface, and blue triangles represent fluid elements, similarly hereinafter.

to form the fluid elements, the fluid nodes (as shown in Fig. 7(a)) must be sorted in an anti-clockwise order (Fig. 7(b)) by minimizing the following expression

$$L = \sum_{i=1}^{n-1} l_i^{i+1} \tag{41}$$

where n is the number of fluid nodes with respect to the hexahedral element (brick element), and l_i^{i+1} represents the distance between fluid node i and $i+1$. Finally, as shown in Fig. 7(c), the fluid elements can be formed by connecting adjacent sorted fluid nodes and sharing a common fluid node 1.

Furthermore, as shown in Fig. 6(b), if the fracture surface contains one or more triangle points used to describe the fracture surface, in addition to intersections of element edges and the fracture surface, these triangle points should also be selected as fluid nodes. Afterwards, fluid elements can be simply determined according to the rules demonstrated in Fig. 7(d)–(f) in which fluid elements are constructed by firstly connecting triangle points, and then connecting triangle points and sorted fluid nodes. Generally, the number of fluid elements n_{fluid} can be quantitatively determined according to the following expression

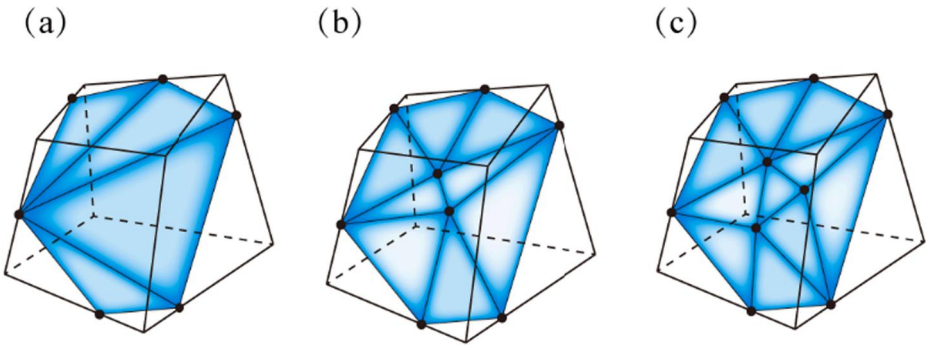

Fig. 8. Illustration of the constructed fluid elements inside the hexahedral elements: (a) 6 intersections of element edges and the fracture surface, no triangle points, and 4 fluid elements constructed; (b) 6 intersections of element edges and the fracture surface, two triangle points, and 8 fluid elements constructed; (c) 6 intersections of element edges and the fracture surface, three triangle points, and 10 fluid elements constructed.

$$n_{fluid} = n_I + 2(n_T - 1) \tag{42}$$

where n_I denotes the number of intersections of element edges and the fracture surface, n_T denotes the number of triangle points used to describe the fracture surface. Take Fig. 8 for example, in Fig. 8(a) n_I equals 6, n_T equals 0, then 4 fluid elements are constructed; in Fig. 8(b) n_I equals 6, n_T equals 2, then 8 fluid elements are constructed; in Fig. 8 (c) n_I equals 6, n_T equals 3, then 10 fluid elements are constructed.

It should be noted that if the area A_e of a fluid element satisfies $A_e \leqslant \varepsilon^e_{tol}\overline{A}_e$, then this fluid element will be degraded to a single fluid node in this study. $\overline{A}_e$ stands for the average area of all fluid elements and ε^e_{tol} is taken as 10^{-4}. After obtaining the fluid elements, the fluid pressure can be applied to the enriched DOFs by performing numerical integration over the entire area of the discrete fluid domain.

For elements intersected by the fracture front, triangle points used to describe the fracture front (i.e., the fracture front vertex), as well as intersections of the fracture front edges and brick element faces should all be selected as fluid nodes. As shown in Fig. 9, fluid node 4 is located at the fracture front vertex, fluid nodes 3 and 5 are located at the intersections of the fracture front edges and brick element face 2 and face 1, respectively, and four fluid elements are constructed in this example. For more complex geometrical cases involving triangle points of the fracture surface, fluid elements can also be easily determined according to the rules depicted in Fig. 9 in conjunction with the strategy presented in the previous paragraph. The number of fluid elements n_{fluid} is determined by

$$n_{fluid} = n_I + n_V + 2(n_T - 1) \tag{43}$$

where n_V denotes the number of fracture front vertex.

3.3. Selection of enriched elements

There are two kinds of enriched elements: the Heaviside enriched elements and the tip enriched elements. In general, there exist two ways to choose tip enriched elements: topological enrichment and geometrical enrichment. For the former, only elements intersected by the fracture front are enriched. For the latter, however, elements whose all nodes are in a fixed area (that is, the distance r_f from the node to fracture front segments satisfies $r_f < r_e$, where r_e is the enrichment radius) are all enriched. To gain a better convergence rate (Agathos et al., 2016), geometrical enrichment is adopted in this paper. For the sake of improving the efficiency of the algorithm, brick elements which contain triangle points, fracture front vertexes, or triangle edges are selected and saved once the newly formed fracture front is available. Hence, the inefficient brute-force search can be avoided. For a certain brick element, the algorithm to determine whether to enrich it or not is summarized as Algorithm 1.

Algorithm 1: An algorithm to determine whether to enrich a brick element or not.

Step 1	If the brick element contains fracture front vertex, then the brick element should be marked as tip enriched element and go to Step 5. If not, go to Step 2.
Step 2	Check if the fracture front intersects the faces of the brick element according to the segment/triangle intersection algorithm (Jiménez et al., 2010). If yes, the element should be marked as tip enriched element and go to Step 5. If not, go to Step 3.
Step 3	Let l_i^j be the signed distance (Algorithm 2) from node i to fracture j. The element should be selected as Heaviside enriched element and go to Step 5 if $max\left(l_i^j\right) \cdot min\left(l_i^j\right) < 0$ (for i varying from 1 to 8, j varying from 1 to the number of fractures) is satisfied. If not, go to Step 4.

(*continued on next page*)

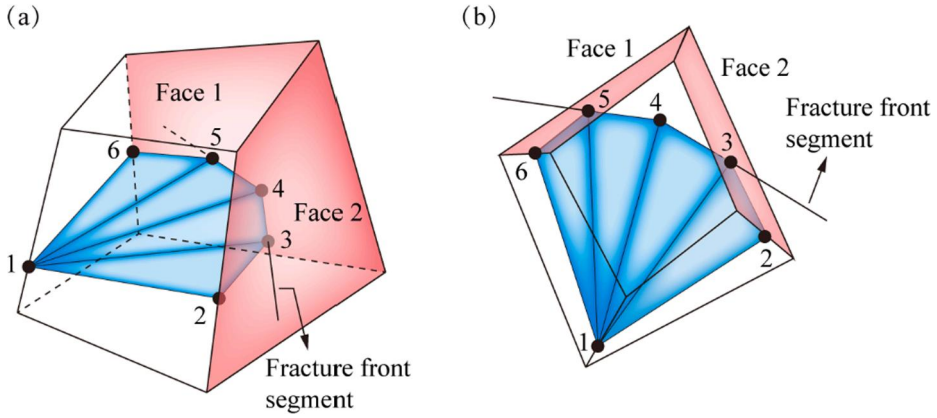

Fig. 9. Construction of fluid elements for the case where the fracture surface contains a fracture front vertex, wherein (a) is the side view and (b) is the top view. Faces colored in red represent the faces of the brick element. Triangles colored in blue represent fluid elements.

(*continued*)

Step 4	Loop over nodes of the brick element, calculate the minimum distance r_f^i from node i ($i = 1,\ldots,8$) to all fracture front segments. If $min\left(r_f^i\right) < r_e$, then the element should be chosen as tip enriched element. Go to Step 5.
Step 5	End.

Calculation of signed distance d_{sign} from a point P (node or Gauss point) to a fracture surface composed of triangle patches is a very crucial part for the selection of Heaviside enrichment elements and the element integration. For a given element, the calculation procedure is summarized as Algorithm 2.

Algorithm 2: Calculation of the signed distance from a point P (node or Gauss point) to a fracture surface composed of triangle patches.

Step 1	If the element contains a triangle point P^T (as depicted in Fig. 10 (a)), then calculate the signed distance from P to all triangles (T_1 to T_n) which share point P^T according to Algorithm 3, and then go to Step 4. If no, go to Step 2.
Step 2	If the element contains any triangle edge E^T (as depicted in Fig. 10(b) which contains two triangle edges E_1^T and E_2^T), then calculate the signed distance $d_{sign}^{S_i}$ from P to all subregions (S_1 to S_n) according to Algorithm 4, and then go to Step 4. If no, go to Step 3.
Step 3	Calculate the signed distance from P to the fracture surface, as illustrated in Fig. 10(c). Go to Step 4.
Step 4	End.

Algorithm 3: Calculation of the signed distance for cases in which the fracture surface contains triangle point and edges.

Step 1	For each triangle, calculate the signed distance $d_{sign}^{T_i}$ from point P to triangle T_i (Appendix A). and check whether the foot of the perpendicular P' lies inside T_i (Appendix A). Go to Step 2.
Step 2	Define a triangle set T^* composed of triangles whose foot of the perpendicular lies inside the triangle patch. If T^* is non-empty, then d_{sign} is the minimum value of $d_{sign}^{T_i}$ where $T_i \subset T^*$, and go to Step 4. If T^* is empty, go to Step 3.
Step 3	Calculate the average normal of all triangles $\overline{\mathbf{n}}_T = \sum_{i=1}^{n} \mathbf{n}_T^i / n$, then d_{sign} can be obtained by calculating the signed distance from P to the spatial plane with normal $\overline{\mathbf{n}}_T$ and passing through P^T. Go to Step 4.
Step 4	End.

Algorithm 4: Calculation of the signed distance for cases in which the fracture surface contains triangle edges but no triangle point.

Step 1	Divide each subregion (a spatial polygon) into a number of triangles, and calculate the signed distances to triangles. Go to Step 2.
Step 2	Define a subregion set S^* composed of subregions whose foot of the perpendicular lies inside the triangle patch. If S^* is non-empty, then d_{sign} is the minimum value of $d_{sign}^{S_i}$ where $S_i \subset S^*$, and go to Step 4. if S^* is empty, go to Step 3.
Step 3	Calculate the average normal of subregions ($\overline{\mathbf{n}}_S = \sum_{i=1}^{\widehat{n}} \mathbf{n}_S^i / \widehat{n}$, where $\widehat{n}$ indicates the number of subregions sharing the edge E_i^T) which share the triangle edge E_i^T. Calculate the signed distance $d_{sign}^{E_i^T}$ from P to the spatial plane with normal $\overline{\mathbf{n}}_S$ and passing through E_i^T. $d_{sign} = min\left(d_{sign}^{E_i^T}\right)$. Go to Step 4.
Step 4	End.

(*continued on next column*)

(*continued*)

3.4. Partitioning the enriched elements with arbitrary discontinuities

Once the enriched elements are obtained, they are subdivided into sub-cells (tetrahedral elements) aligned with the discontinuity for numerical integration which is of great importance to achieve better accuracy and optimal convergence. Similar to the identification of the fluid elements, the procedure to partition enriched elements with arbitrary discontinuities varies depending on the situation whether the element

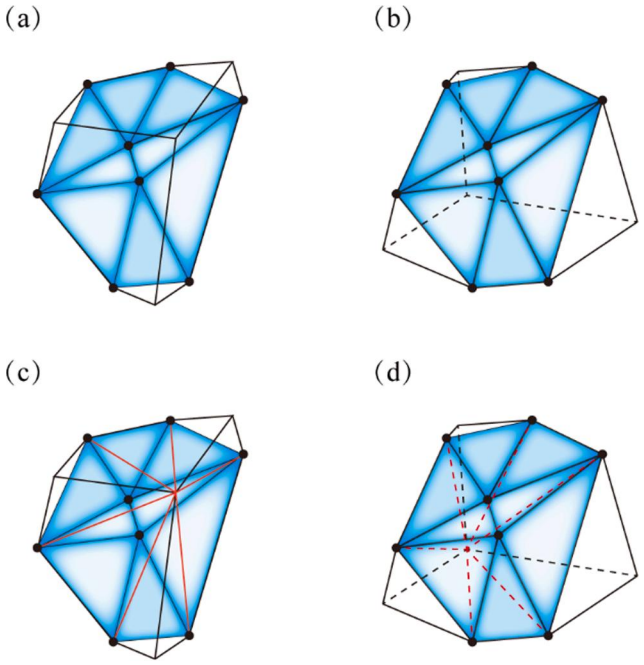

Fig. 11. Subdivision of an enriched element containing no fracture front. (a) the upper sub-element; (b) the lower sub-element; (c) tetrahedrons of the upper sub-element; (d) tetrahedrons of the lower sub-element.

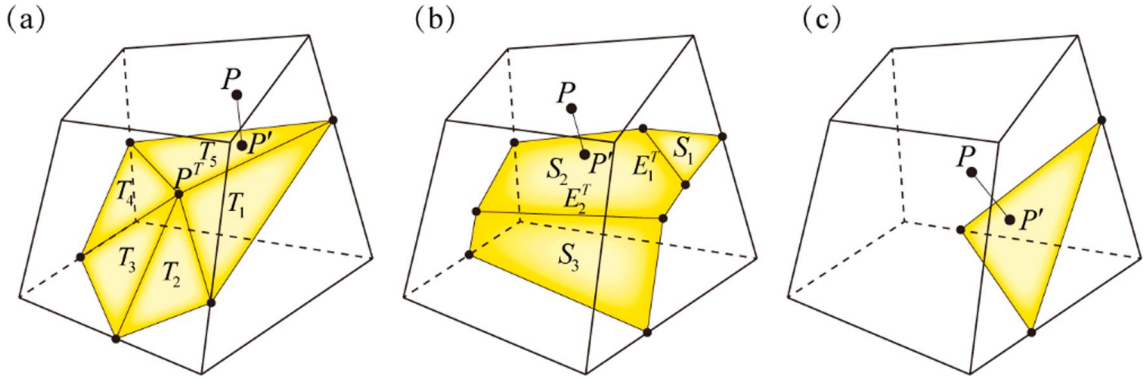

Fig. 10. Calculation of the sighed distance from point P to the fracture surface which contains (a) a triangle point and edges; (b) triangle edges; (c) neither triangle point nor edge.

includes a piece of the crack front or not.

For brick elements that contain no fracture front, after obtaining the fluid elements, the sub-elements and tetrahedrons for numerical integration can be obtained according to the following procedure (take the case in Fig. 8(b) for example):

- Divide the brick element into two sub-elements by the surface composed of fluid elements, as shown in Fig. 11(a) and (b) where both sub-elements have 14 flat faces.
- If the flat faces contain more than 3 vertexes, then divide them into flat triangles by connecting the vertexes and sharing a common vertex, as shown in Fig. 11(c) and (d) where both sub-elements have 20 triangle faces.
- For each sub-element, create a new point by computing the arithmetic mean of the coordinates constituting all triangle faces of each sub-element.
- Construct tetrahedrons by connecting the newly created point and each triangle face. For the case shown in Fig. 11, the number of tetrahedrons for both sub-elements is 20.

For brick elements that contain fracture fronts, the tetrahedrons can be obtained according to the following procedure in which another complementary cutting procedure has to be performed (take the case in Fig. 9 for example):

- Extend the original surface (composed of blue triangles shown in Fig. 12) to form a cutting surface that is able to completely split the brick element. After the extension, the added triangles are colored in orange as shown in Fig. 12(a).
- Divide the brick element into two sub-elements by the cutting surface, as shown in Fig. 12(b) and (c) where each sub-element has 11 faces.
- Divide the flat faces which contain more than 3 vertexes into triangles by connecting the vertexes and sharing a common vertex as illustrated by the red lines in Fig. 12(a) and (c).
- For each sub-element, create a new point by computing the arithmetic mean of the coordinates constituting all triangle faces of each sub-element.
- Construct tetrahedrons by connecting the newly created point and each triangle face.

Finally, the numerical integration of the brick element containing discontinuity (Fig. 8 (b)) can be performed through 40 tetrahedral elements with 4 Gauss integration points (Loehnert et al., 2011) for each tetrahedral element. Besides, for the brick element presented in Fig. 9, the resulting number of tetrahedral elements is 32. It should be noted that nodes on each face of the tetrahedron must be sorted in an anticlockwise direction in order to avoid the negative volume error.

4. Numerical examples

The theoretical model and simulation methods proposed in this paper have been programmed into an in-house program called PhiPsi (http://phipsi.top). Several examples are presented to show the efficiency, robustness, and applicability of the presented method. The computer used to perform the numerical examples has an AMD 3950X CPU (16 physical cores) and 128 GB memory space. It should be noted that since the process of fracture nucleation has not been considered, the initial cracks in all examples are given as known at specified locations, for example, the center of the geometric model. Besides, in this paper, geometric models are all discretized with non-uniform meshes. More specifically, fine meshes are employed within a predetermined region that is in the vicinity of the initial fracture. Thus, remeshing is required only when the hydraulic fractures propagate beyond the refined region, which in fact does not occur in all examples because the refined region is large enough to cover the propagated fracture.

4.1. Inclined penny-shaped fracture subjected to a tensile load

The first example is aimed to investigate the convergence rate of the proposed method and validate the accuracy of SIFs calculated using the displacement extrapolation method with high-order terms. As illustrated in Fig. 13, an inclined penny-shaped fracture is located at the center of a

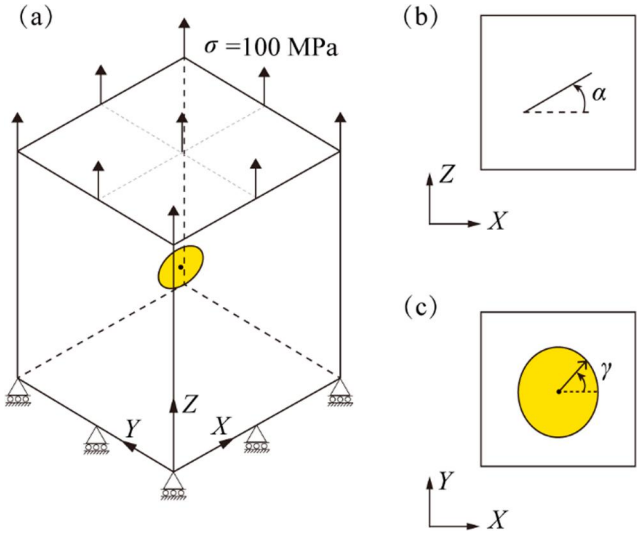

Fig. 13. (a) Schematic of a cubic domain which contains an inclined penny-shaped fracture; (b) The front-view (in the *X-Z* plane) and (c) the top view (in the *X-Y* plane) of the fracture. The size of the fracture is magnified in (b) and (c).

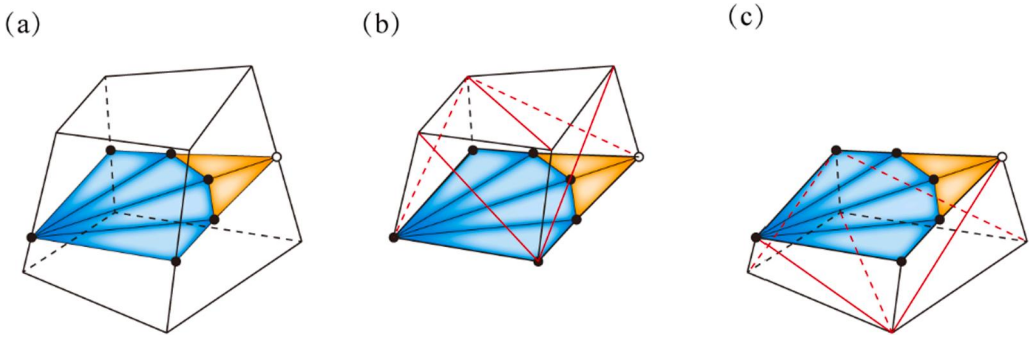

Fig. 12. Subdivision of an enriched element containing fracture front. (a) the enriched element with extended faces (colored in orange); (b) tetrahedrons of the upper sub-element; (c) tetrahedrons of the lower sub-element.

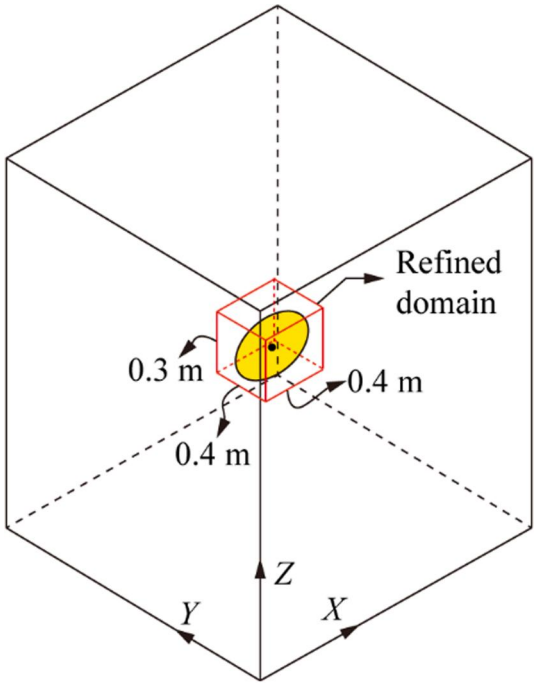

Fig. 14. Illustration of the refined domain.

cuboid of size 2 × 2 × 2 m. The angle α between the fracture surface and the horizontal surface is $\pi/6$. The initial radius a of the fracture equals 0.1 m. r_e for the geometrical enrichment is taken as 0.04 m. The tensile stress σ_{zz} applied on the top surface of the domain is 100 MPa. Young's modulus E and Poisson's ratio ν are 20 GPa and 0.3, respectively. As shown in Fig. 14, the domain with a size of 0.4 × 0.4 × 0.3 m (in x, y, and z directions, respectively) located at the model center is discretized with four different mesh densities, i.e., 0.02 × 0.02 × 0.02 m (mesh case 1), 0.015 × 0.015 × 0.015 m (mesh case 2), 0.01 × 0.01 × 0.01 m (mesh case 3), and 0.005 × 0.005 × 0.005 m (mesh case 4). As a consequence, the minimum element edge lengths $h_{\min}$ are 0.02 m, 0.015 m, 0.01 m, and 0.005 m for mesh cases 1 to 4, respectively. The number of elements along the x direction of the refined domain is 20, 27, 40, and 80, respectively. The number of total elements for cases 1 to 4 are 19,600, 36,750, 92,160, and 542,080, respectively. With the increase of the mesh density, a dramatic increase of elements number can be clearly seen. Fortunately, the enriched DOFs constitute only a portion (14.7%, 13.5%, 11.7%, and 8.8% for mesh case 1 to 4, respectively) of the total DOFs, as shown in Fig. 15. More importantly, the ratio of enriched DOFs decreases with the increase of the total DOFs. Hence, in virtue of the reduction technique, the DOFs involved in the solution process can be reduced.

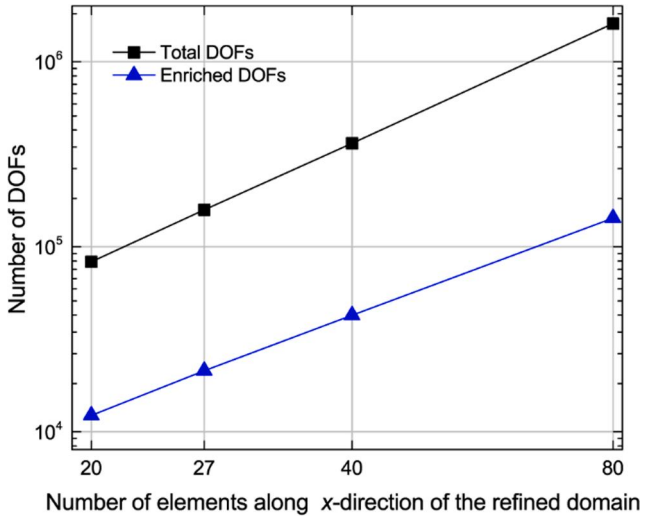

Fig. 15. Number of total DOFs and enriched DOFs for mesh case 1 to 4.

4.1.1. L_2 norm and energy norm of error

In this example, because there is no fluid pressure, the discrete fluid flow equation (Eq. (18)) is of no concern, and the nodal displacement vector can be determined by solving Eq. (14) in the absence of vector **P**. Convergence rates of four different methods including XFEM, XFEM-High order terms (the proposed method), and XFEM-High order terms-WR (for the description of acronyms, see Table 1) are tested in this example. The L_2 norm of the error and the energy norm of the error are defined as, respectively

$$\mathrm{err}_{L_2} = \frac{\left(\int_\Omega \left(\mathbf{u}_{Ref} - \mathbf{u}\right)^T \left(\mathbf{u}_{Ref} - \mathbf{u}\right) d\Omega\right)^{1/2}}{\left(\int_\Omega \mathbf{u}_{Ref}^T \mathbf{u}_{Ref} d\Omega\right)^{1/2}} \tag{44}$$

$$\mathrm{err}_E = \frac{\left(\int_\Omega \left(\boldsymbol{\varepsilon}_{Ref} - \boldsymbol{\varepsilon}\right)^T \mathbf{D} \left(\boldsymbol{\varepsilon}_{Ref} - \boldsymbol{\varepsilon}\right) d\Omega\right)^{1/2}}{\left(\int_\Omega \boldsymbol{\varepsilon}_{Ref}^T \mathbf{D} \boldsymbol{\varepsilon}_{Ref} d\Omega\right)^{1/2}} \tag{45}$$

where $\mathbf{u}_{Ref}$ and $\boldsymbol{\varepsilon}_{Ref}$ denote reference displacement fields and strain tensors obtained from FEM, $\mathbf{u}$ and $\boldsymbol{\varepsilon}$ denote corresponding results obtained using the proposed method. In Fig. 16, the influence of the mesh density on err_{L_2} and err_E is investigated. It can be seen that the tip enrichment functions with high-order terms show better convergence rates and improved accuracy for both the L_2 norm and the energy norm of error, compared to the conventional XFEM with 4 tip enrichment terms and topological enrichment. Moreover, it should be noted that the reduction technique has no influence on the simulation results, just as demonstrated in previous work (Shi et al., 2017).

4.1.2. Stress intensity factors

In this section, the proposed method (XFEM-High order terms) is adopted to evaluate the extraction method of SIFs proposed in Section 2.7. r_c and Δr are taken as 0.01 m and 0.1 h_{min}, respectively. The relative error of SIF of mode-i is defined as

$$\mathrm{err}_K^i = \frac{\left(\sum_{j=1}^{n_K} \left(K_i^j - \widehat{K}_i^j\right)^2\right)^{1/2}}{\left(\sum_{j=1}^{n_K} \left(\widehat{K}_i^j\right)^2\right)^{1/2}} \tag{46}$$

where n_K is the number of calculation points of SIFs along the fracture front, K_i^j and $\widehat{K}_i^j$ denote, respectively, numerical and analytical SIF value of mode-i at calculation point j. The analytical solutions of mode I, II, and III SIFs are available (Duflot, 2006) and can be written as

$$\widehat{K}_1 = 2\sigma cos^2\alpha \sqrt{\frac{a}{\pi}} \tag{47}$$

Table 1
Acronyms of tested methods.

Acronym	Method description
XFEM	XFEM with 4 tip enrichment terms and topological enrichment
XFEM- High order terms	XFEM with 10 tip enrichment terms
XFEM- High order terms-WR	XFEM with 10 tip enrichment terms but Without the Reduction technique

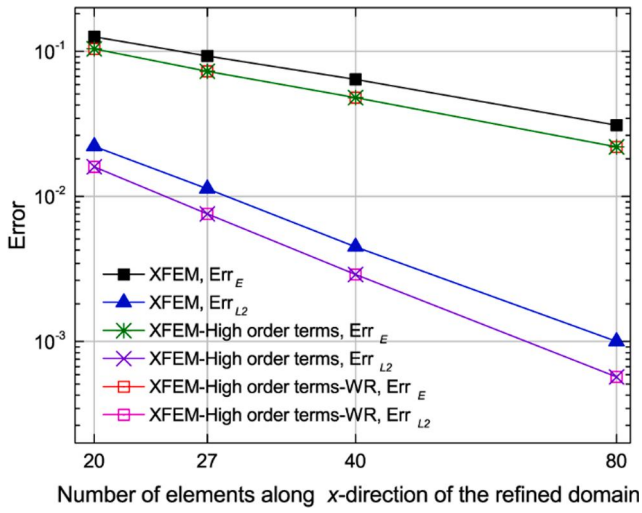

Fig. 16. L_2 norm of the error and the energy norm of the error versus number of elements along the long side direction of the refined mesh zone.

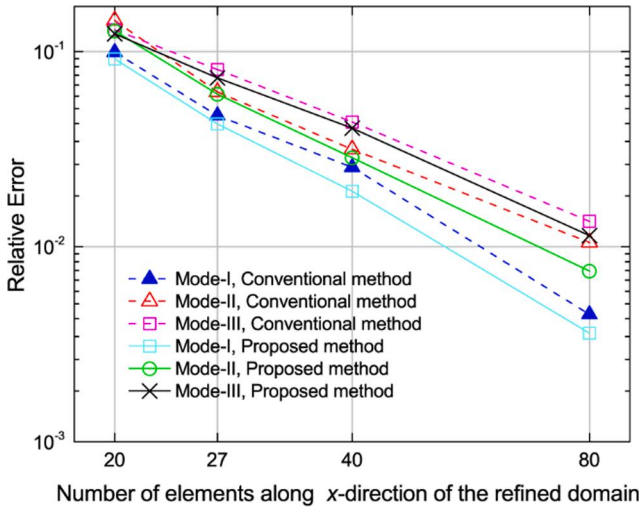

Fig. 17. Relative errors of the SIFs with various mesh densities.

$$\widehat{K}_{\mathrm{II}} = -\frac{4}{2-\nu}\sigma sin\alpha cos\alpha\sqrt{\frac{a}{\pi}}sin\gamma \tag{48}$$

$$\widehat{K}_{\mathrm{III}} = -\frac{4(1-\nu)}{2-\nu}\sigma sin\alpha cos\alpha\sqrt{\frac{a}{\pi}}cos\gamma \tag{49}$$

where γ is the fracture front angular position where the SIFs are calculated, just as depicted in Fig. 13(c).

The relative errors of the calculated SIFs with comparison to the analytical solutions are given in Fig. 17. With the refinement of the mesh, the errors gradually decrease. It can be noticed that the proposed displacement extrapolation method with high-order terms (denoted by "Proposed method" in the figure) can predict the SIFs with higher accuracy compared to the conventional displacement extrapolation method (denoted by "Conventional method" in the figure).

4.2. Growth of a penny-shaped fracture under constant pressure

The second example verifies the computational methodology presented in Section 3 and the crack propagation model presented in Section 2.7. The effect of element size will also be investigated in this example. A cubic domain has a size of 50 × 50 × 50 m, and the initial

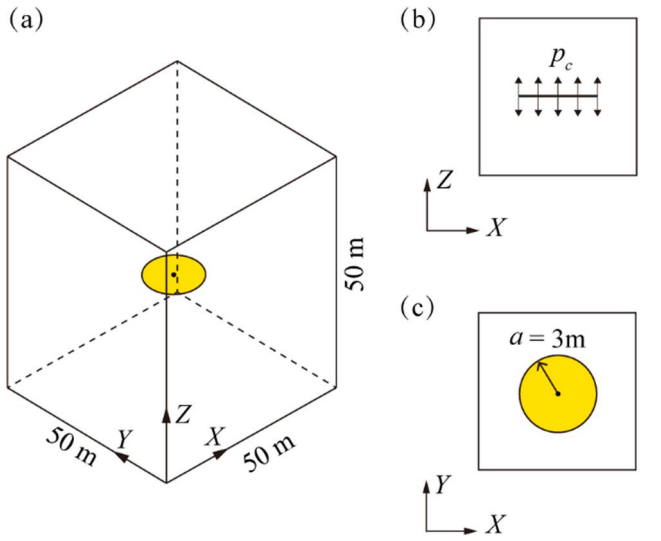

Fig. 18. (a) Schematic of a cubic domain which contains an initial penny-shaped fracture; (b) The front-view (in the *X*-*Z* plane) and (c) the top view (in the *X*-*Y* plane) of the fracture. The size of the fracture is magnified in (b) and (c).

penny-shaped crack, which is horizontally located at the center of the domain and filled with fluid of constant pressure, has a radius of $a = 3$ m, as shown in Fig. 18. All of the domain boundaries are fixed. Young's modulus E, Poisson's ratio ν, and fracture toughness K_{Ic} are given values of 20 GPa, 0.3, and 2 MPa·m$^{1/2}$, respectively. Similar to Fig. 14, a refined domain with a size of 10 × 10 × 5 m is located at the model center. The sizes of elements within the refined domain are 0.5 × 0.5 × 0.5 m (mesh case 1) and 0.25 × 0.25 × 0.25 m (mesh case 2), and the model has been meshed into 10,200 and 43,800 hexahedral elements in total, respectively. r_e is taken as 1.5 m. For mesh case 1, the discrete initial geometrical fracture surface and the local coordinate systems at the discrete points on the fracture front are shown in Fig. 19. In addition, the number of fluid elements of the initial fracture is 298, as shown in Fig. 20.

The necessary pressure p_c required to propagate the fracture and the volume V_c of the injected fluid can be obtained according to the following analytical solutions (Abé et al., 1976):

$$p_c = \sqrt{\frac{K_{\mathrm{Ic}}^2\pi}{4a}} \tag{50}$$

$$V_c = \sqrt{\frac{64a^5K_{\mathrm{Ic}}^2\pi(1-\nu^2)^2}{9E^2}} \tag{51}$$

In this example, since constant pressure is applied, the discrete fluid flow equation (Eq. (18)) is of no concern, and the nodal displacement vector can be obtained by directly solving Eq. (14). The comparison of the analytical solution (Eq. (50)) and the numerical solution of the fluid pressure (p_c) required to propagate the fracture of different radius is shown in Fig. 21, from which a good agreement can be observed. For mesh case 1, the error equals 4.4% and 1.9% when the radius equals 3 m and 6 m, respectively. In addition, for mesh case 2, the error can be further reduced to 1.7% and 0.8%, respectively. The volume of the penny-shaped fracture at different radius is shown in Fig. 22, where again good agreement between theory (Eq. (51)) and simulation results can be seen. From Figs. 21 and 22, it can be concluded that the presented XFEM enrichment scheme for the fracture within hexahedral solid elements is able to capture the discontinuous features of the fluid-driven fracture, the triangular fluid elements shown in Fig. 20 are sufficient to describe fluid pressure, and the displacement extrapolation method of SIFs calculation is accurate enough for the 3D fracture under the action

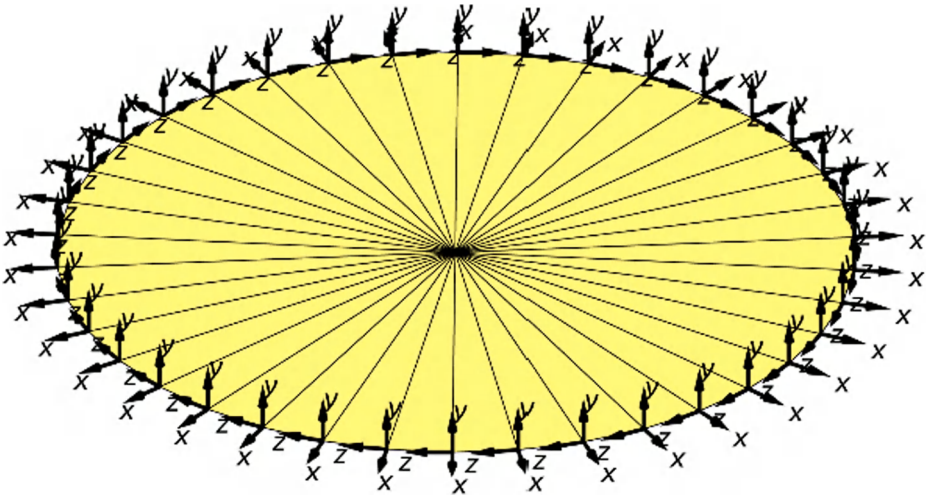

Fig. 19. Discrete initial geometrical fracture surface. The local Cartesian coordinate systems at the vertexes of fracture front are also shown.

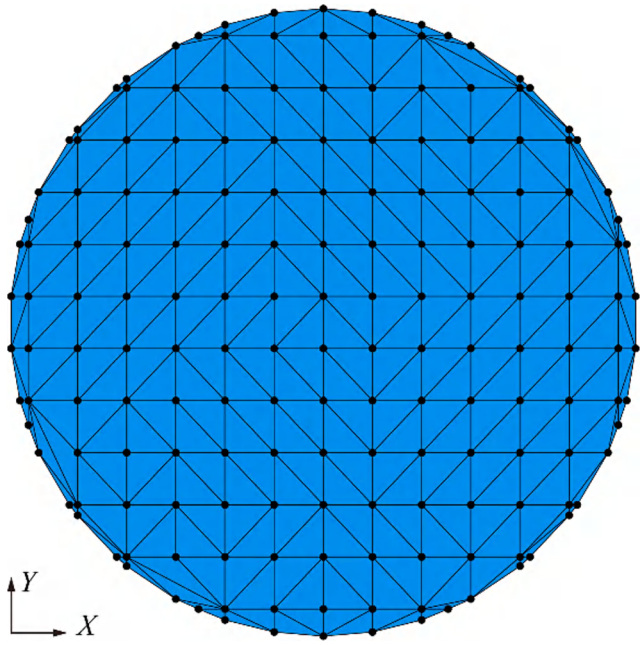

Fig. 20. Fluid elements of the initial fracture for mesh case 1. The black dots represent fluid nodes.

of fluid pressure.

4.3. Growth of a penny-shaped fracture under fracturing fluid

In this example, a benchmark problem which has available asymptotic analytical solutions (Appendix B) will be studied to verify the fluid-solid coupling model presented in Section 2.5. Both toughness-dominated and viscosity-dominated fracturing (Savitski and Detournay, 2002) are studied by setting the fluid viscosity to 0.0001 Pa·s and 0.1 Pa·s, respectively. A penny-shaped fracture is horizontally placed at the center of the 100 × 100 × 100 m cubic domain. The initial radius a of the fracture is equal to 1.5 m. The mesh is locally refined with 0.25 × 0.25 × 0.25 m elements within the refined region with a size of 23 × 23 × 2 m around the fracture. The total number of brick elements is 97,780. Fluid is pumped into the fracture center at a rate of 0.01 m^3/s. Material properties of rock formation are given values of $E = 17$ GPa, $\nu = 0.25$, and $K_{Ic} = 2$ MPa·$m^{1/2}$. The pumping time is 20 s.

The time evolution of fracture radius, the final fracture opening as

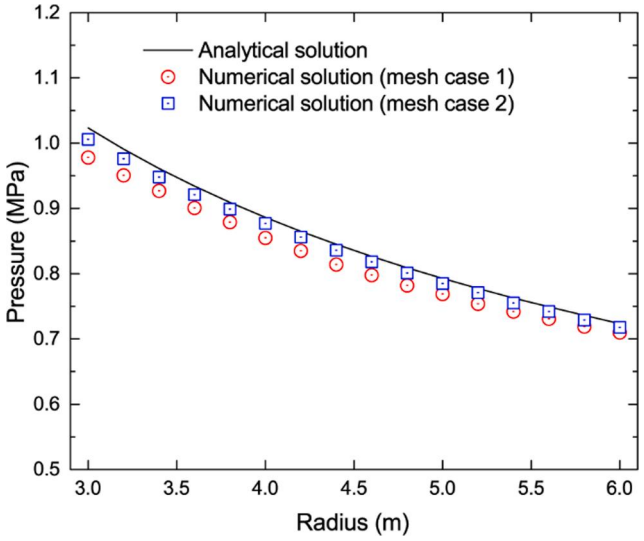

Fig. 21. Fluid pressure required to propagate the penny-shaped fracture at different radius.

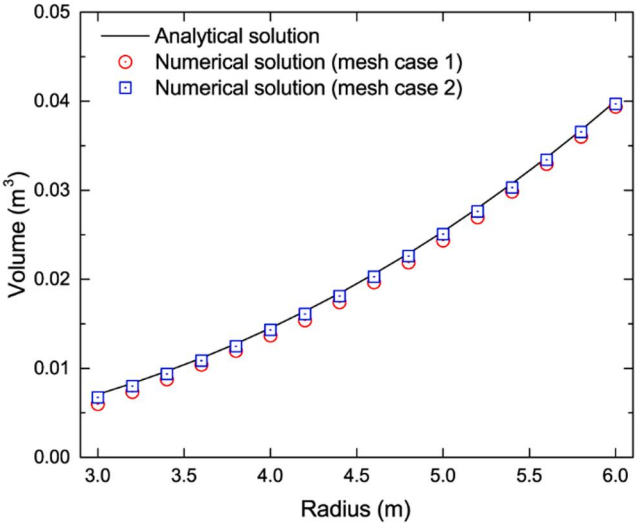

Fig. 22. Volume of the penny-shaped fracture at different radius.

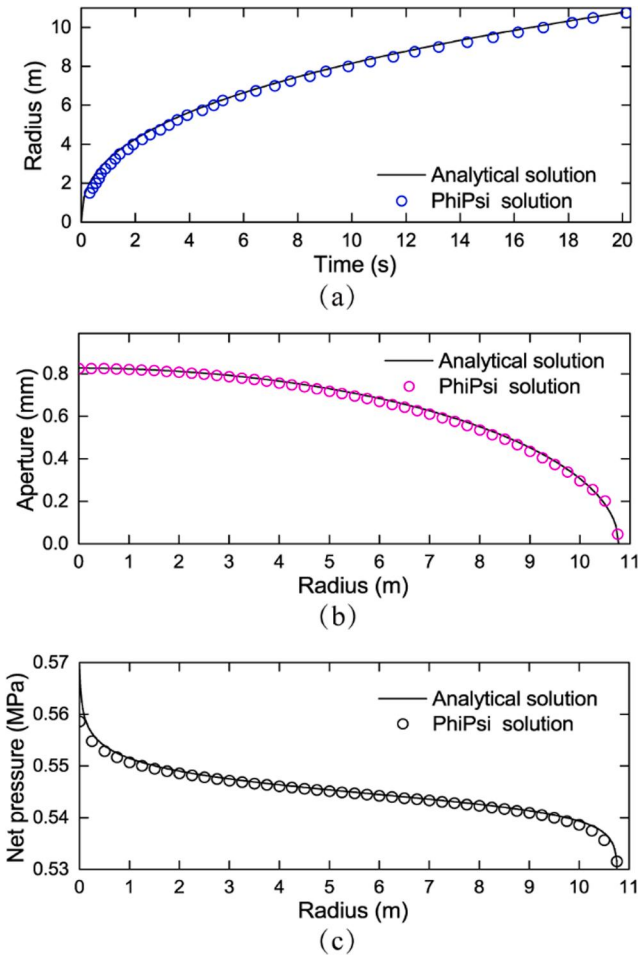

Fig. 23. Results of the toughness-dominated fracturing of a penny-shaped fracture: (a) time evolution of fracture radius; (b) final fracture opening; (c) final net pressure.

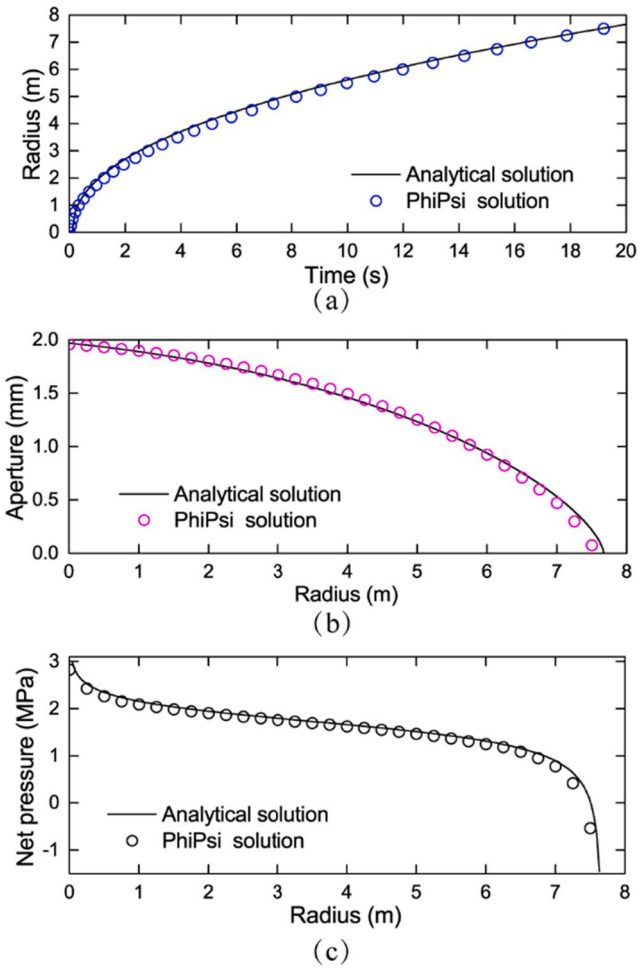

Fig. 24. Results of the viscosity-dominated fracturing of a penny-shaped fracture: (a) time evolution of fracture radius; (b) final fracture opening; (c) final net pressure.

well as the net pressure along the radius are presented in Figs. 23 and 24 for the toughness-dominated simulation and the viscosity-dominated simulation, respectively. Good agreements can be seen from both figures, which indicates that the proposed fluid-solid coupling model is capable of 3D hydraulic simulation for both low and high viscosity fracturing fluid. It is worthwhile noting that the singularities of net pressure near the fracture center and the fracture front, which are consistent with the analytical solutions, are caused by the point source assumption and the zero-lag assumption, respectively. It can also be found that the radius of the final fracture of the viscosity-dominated case is much smaller compared to the toughness-dominated case. This is because the majority of the energy has been dissipated during the viscous flow process rather than the fracturing process. Additionally, it should be noted that the obtained results are smooth and continuous rather than in a stepwise and oscillating manner observed in other simulation studies (Feng and Gray, 2017; Cao et al., 2018; Shovkun and Espinoza, 2019; Milanese et al., 2016; Secchi and Schrefler, 2014). This is because the rock formation is assumed to be impermeable media in this paper. Meanwhile, the fluid exchange between the fracture and the surrounding (leek-off) is ignored. According to the possible mechanisms that induce the stepwise advancements, basic requirements including permeable rock formation and fluid leak-off have not been satisfied (Feng and Gray, 2017; Milanese et al., 2016; Pizzocolo et al., 2013). On the other hand, the maximum crack increment length is predetermined in this study (see Eq. (32)), and the advancement algorithm does not

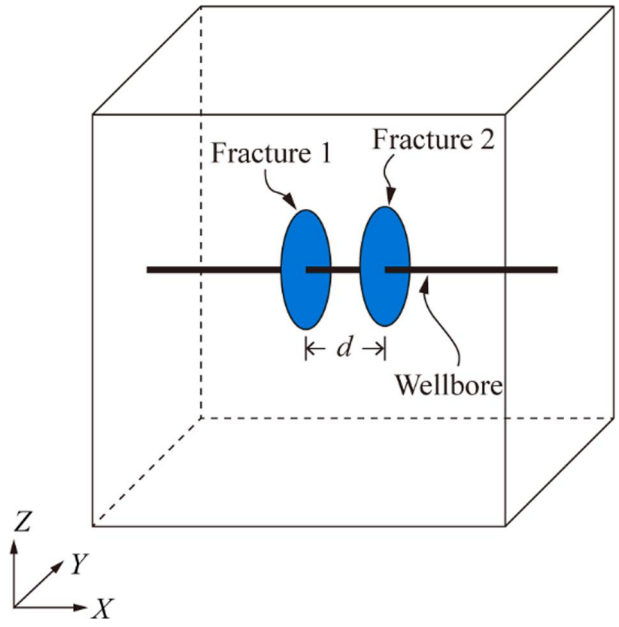

Fig. 25. Schematic of a cubic domain that contains two initial parallel penny-shaped fractures.

allow for displacement jumps within a time step. However, the independence between the advancement algorithm and the time-stepping algorithm is of paramount importance if stepwise advancement has to be obtained (Cao et al., 2018). This is believed to be another reason for the failure of the proposed model to capture the stepwise advancement phenomenon.

4.4. Growth of two close penny-shaped fractures

In this example, the accuracy and efficiency of the proposed numerical model will be demonstrated through an example in which two initial parallel penny-shaped fractures of 1 m radius are vertically located at the center of a 100 × 100 × 100 m cubic domain, as shown in Fig. 25. Besides, the influence of the reduction technique on consumed CPU time is also investigated. The distance between fractures d is taken as 5 m, 10 m, and 15 m, respectively. The in-situ stress in all three directions (x, y, and z) is 10 MPa. The fluid of 0.1 Pa·s viscosity is simultaneously injected into both fractures at a rate of 0.01 m^3/s. The pressure loss along the horizontal well has not been considered. Point source boundary condition is assumed because of the negligible size of the wellbore compared to the size of fractures. We choose Young's modulus $E = 20$ GPa, Poisson's ratio $\nu = 0.2$, and fracture toughness $K_{Ic} = 2$ MPa·$m^{1/2}$. The mesh is locally refined with 0.5 × 0.5 × 0.5 m element within the region with a size of 20 × 20 × 20 m around fractures. The total number of brick elements is 123,600. A comparison of the propagation paths between our solution and an existing solution done by Salimzadeh et al. (2017) using the finite element method will be given.

For two adjacent fractures, it will grow away from the other one due to the compressive stress field caused by the opening of the nearby fracture filled with high-pressure fluid. This phenomenon is called the stress shadow effect. As shown in Fig. 26, there is a good agreement of fracture propagation paths between the published results (Salimzadeh et al., 2017) and the present simulation results, indicating that the presented model is capable of predicting the effect of stress shadow between fractures. The cross-section view ($y = 0$) of the stress distribution in x direction is given in Fig. 27. It can be observed that the stress around the fracture front is lower than the in-situ stress, but the stress in the region between fractures is higher than the in-situ stress (i.e., the stress build-up zone or the stress shadow zone). It can also be observed from Fig. 27 that the intensity of the stress shadow decreases with increasing spacing between fractures, which leads to less curving of the fracture propagation paths. The geometrical surface of the final induced fractures of 5 m spacing is shown in Fig. 28. The fracture surfaces are composed of 1988 triangle patches and are completely smooth without any tortuous feature. This conclusion is consistent with the symmetry of this problem and clearly reveals the reliability and accuracy of the proposed approach. Moreover, the fracture opening is shown in Fig. 28 where the maximum value of 0.93 mm arises at the fracture center.

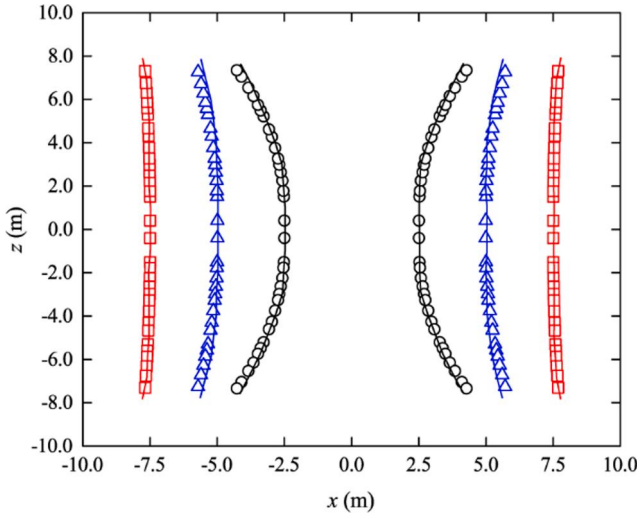

Fig. 26. Effect of the fracture spacing on the fracture propagation paths in a 2D cross-section view ($y = 0$). The black, blue, and red lines represent the paths obtained in the reference (Salimzadeh et al., 2017) with spacing 5 m, 10 m, and 15 m, respectively. The black circles, blue triangles, and red squares represent the paths obtained in the present study with spacing 5 m, 10 m, and 15 m, respectively.

The CPU time for the case where d equals 5 m is presented in Fig. 29. For the first two propagation steps, the CPU time with the reduction technique is longer than the one without the reduction technique because some extra operations related to DOFs decomposition need to be carried out at the beginning of the simulation. However, the positive effect of the reduction technique on computational efficiency becomes more and more obvious as fractures propagate. As a result, the total CPU time is decreased by 53.5%.

4.5. Growth of a planar fracture: validation against experimental data

In this example, we validate the proposed numerical model and algorithms with laboratory experimental results (Wu et al., 2008) of a planar hydraulic fracture subjected to heterogeneous confining stresses. The experiment was conducted using two unbonded impermeable polymethyl methacrylate (PMMA) blocks of thickness 175 mm and the hydraulic fracture grows along the unbonded interface. As depicted in Fig. 30, the size of the model in x, y, and z directions are 340 mm, 250 mm, and 350 mm, respectively. In-situ stresses in z direction in Zone 1, Zone 2, and Zone 3 are 11.2 MPa, 7.0 MPa, and 5.0 MPa, respectively. The coordinates of the injection point are (0, 0, 0). The radius of the initial circular fracture originated from the injection point is 20 mm. The viscosity of the injected fluid is 30 Pa·s. The fracture toughness on the interface fracture plane is zero and the pure mode-I hydraulic fracture propagation process is in the viscosity-dominated regime. Material parameters E and ν of the PMMA are 3.3 GPa and 0.4, respectively. In the experiment, the fluid is injected in three stages and the injection rate changes with time as follows

$$Q(t) = \begin{cases} 0.9 \times 10^{-3}\text{mL/s}, & 0 < t \leqslant 31\text{ s} \\ 6.5 \times 10^{-3}\text{mL/s}, & 31\text{ s} < t \leqslant 151\text{ s} \\ 2.3 \times 10^{-3}\text{mL/s}, & 151\text{ s} < t \leqslant 701\text{ s} \end{cases} \tag{52}$$

Because the fracture propagates only in mode-I, a thin domain of size 340 × 250 × 12.5 mm (in x, y, and z directions, respectively) around the interface fracture plane is locally refined with 2.5 × 2.5 × 2.5 mm elements. The total number of brick elements is 176,800. r_e for the geometrical enrichment is taken as 7.5 mm.

Comparisons of numerical and experimental fracture footprints at different injection times are presented in Fig. 31. It can be seen that the numerical results agree very well with the experimental results. Furthermore, Fig. 32 gives the evolution of fracture width at (30 mm, 0) which has been experimentally measured by Wu et al. (2008). Again, good agreement between the numerical results and the experimental data can be observed. It is worth noting that a sharp decrease of fracture width can be seen from the numerical results at the end of the second injection stage. However, considering the compliance of the injection system, the real fluid injection rates in the experiment may be different from the expected one as given in Eq. (52). Therefore, the measured fracture width changes smoothly rather than in an abrupt manner compared to the numerical results.

4.6. Mixed-mode growth of an inclined penny-shaped fracture under fracturing fluid

The goal of this example is to show the effects of mode III loading on fracture propagation path and the role of K_{III} in the fracture propagation criterion. The geometric model used here is similar to the one described

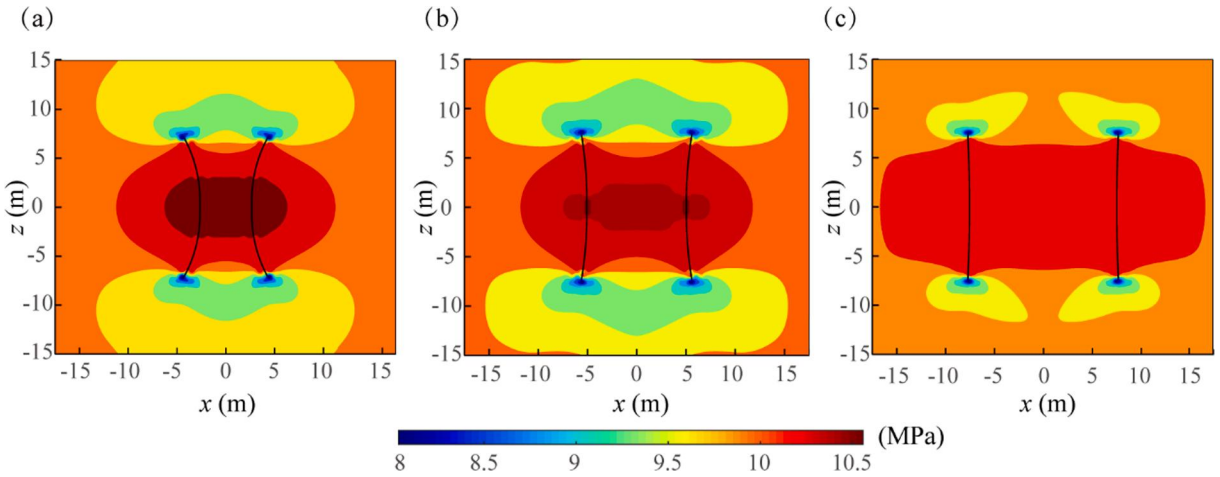

Fig. 27. Cross-section view ($y = 0$) of the stress distribution in $\times$ direction and the geometry of the propagated fractures with initial spacing 5 m (a), 10 m (b), and 15 m (c). Positive values indicate compression stress.

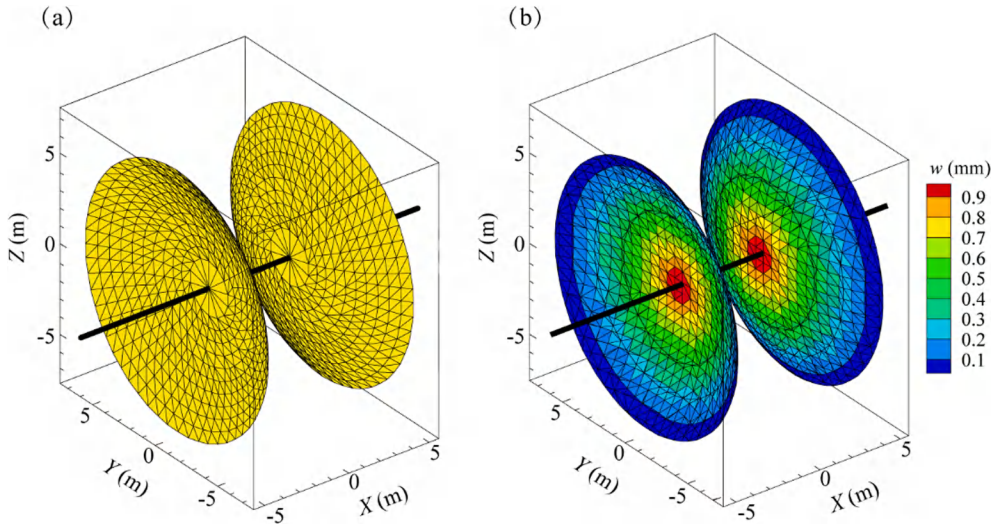

Fig. 28. Geometrical fracture surface and fracturing opening of the final induced fractures of 5 m initial spacing.

in Section 4.1. As illustrated in Fig. 13, an inclined penny-shaped fracture is located at the center of a cuboid of size 150 × 150 × 150 m. The angle α between the fracture surface and the horizontal surface is $\pi/4$. The initial radius a of the fracture equals 2.5 m. The fluid of 0.01 Pa·s viscosity is injected at the fracture center at a rate of 0.01 m^3/s. r_e for the

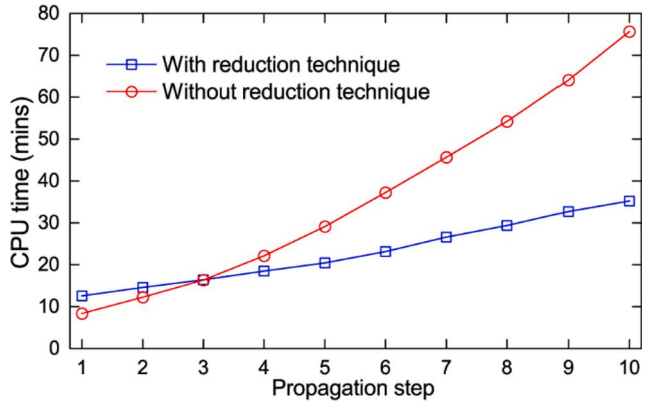

Fig. 29. Consumed CPU time for the case where d equals 5 m. A single CPU process is used in this example.

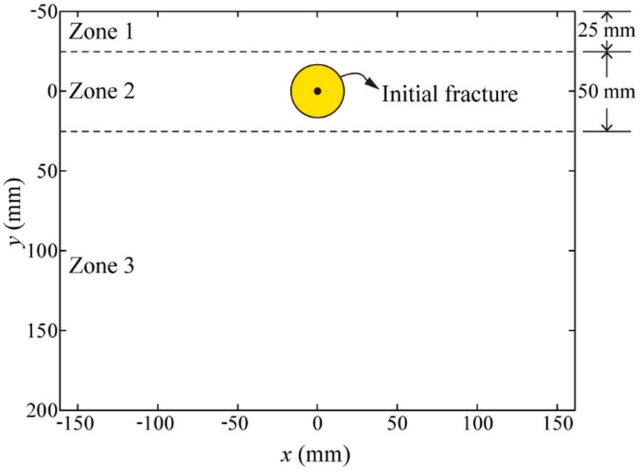

Fig. 30. Schematic of the interface fracture plane of PMMA blocks subjected to heterogeneous confining stresses.

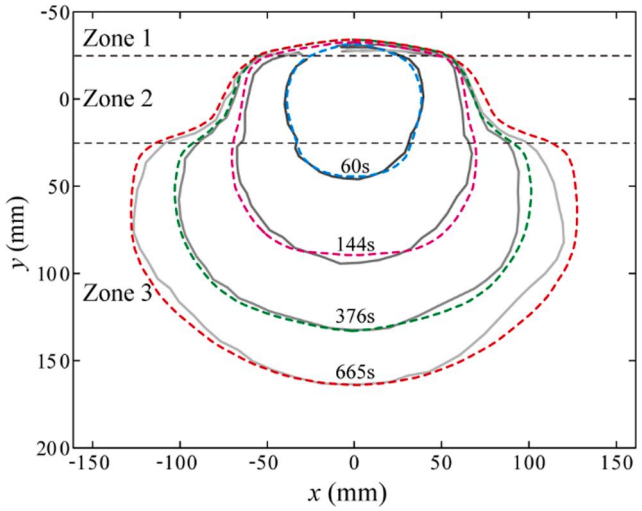

Fig. 31. Numerical and experimental fracture footprints at different injection times. Experimental results (Wu et al., 2008) are denoted by solid lines and numerical results are denoted by dotted line.

geometrical enrichment is taken as 1.05 m. The in-situ stresses σ_{xx}, σ_{yy} and σ_{zz} are 1.0 MPa, 1.0 MPa, and 2.5 MPa, respectively. Material parameters of the rock formation E, ν, and K_{Ic} are 20 GPa, 0.2, and 2 MPa·m$^{1/2}$, respectively. The domain with a size of 15 × 15 × 20 m (in x, y, and z directions, respectively) located at the model center is discretized with a mesh density of 0.35 × 0.35 × 0.35 m. The number of total brick elements is 173,056. The simulation involves 10 propagation steps. Mode III effects on fracture path are investigated by considering $K_{III} = 0$.

Geometrical fracture surfaces after the final propagation step are shown in Fig. 33. In this paper, all fracture modes are taken into account in the adopted Schöllmann's criterion (Schöllmann et al., 2002). However, as discussed in Section 2.7, since it conserves the continuity of the fracture front, this criterion is incapable of reproducing the fracture front segmentation process (Bunger et al., 2017; Ketterij and Pater, 1999). Hence, the resulting fracture surface is smooth and continuous without segmentation on the fracture front. Details of the fracture reorientation paths and the reorientation angles are presented in the cross-section view shown in Fig. 34. The reorientation angle ϕ_1 (61.3°) with K_{III} effects is 16.8% larger than ϕ_2 (52.5°) without K_{III} effects. The Schöllmann's criterion considering K_{III} effects gives a more tortuous path and is more likely to provide a planar mode I crack growth as the

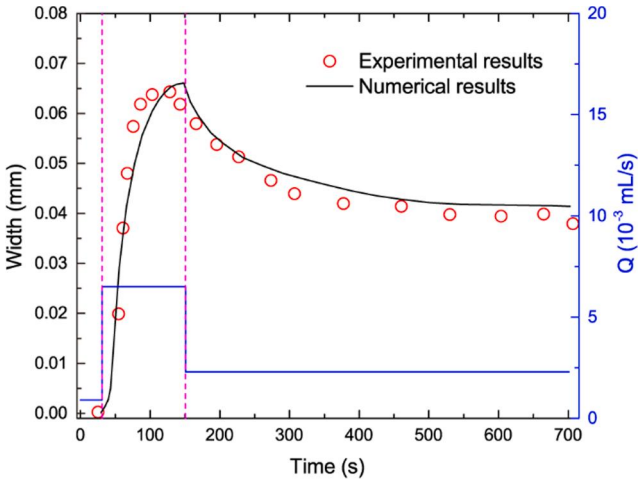

Fig. 32. Evolution of fracture width at a measurement point located at (30 mm, 0). The injection schedule is also shown.

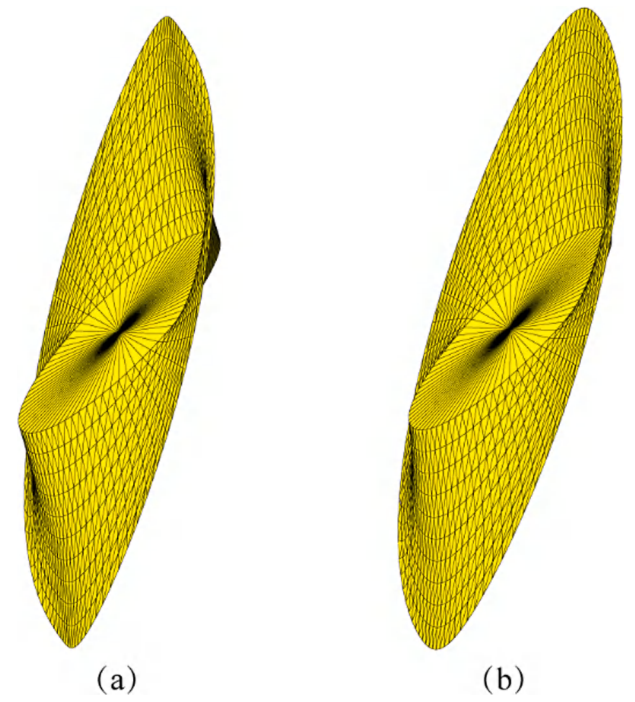

Fig. 33. Geometrical fracture surfaces after the final propagation step: (a) with K_{III} effects; (b) without K_{III} effects.

fracture propagates (Pereira et al., 2010) compared to the case without K_{III} effects. Fig. 35 depicts the evolution of borehole pressure over time with and without K_{III} effects. The final borehole pressure of the case without K_{III} effects is 1.33 MPa and is 5.7% lower than 1.41 MPa of the case with K_{III} effects. Besides, Fig. 36 shows the time evolution of fracture width at the injection point with and without K_{III} effects. The final fracture width of the case without considering K_{III} effects is 1.21 mm and is 8.3% lower than 1.32 mm of the case with K_{III} effects. According to the results presented in this section, it can be concluded that mode III effects cannot be ignored in a hydraulic fracturing simulation. In fact, the effects of K_{III} are more significant if the fracture front segmentation is reproduced in a numerical model (Huang et al., 2013). This will be further investigated in the future study.

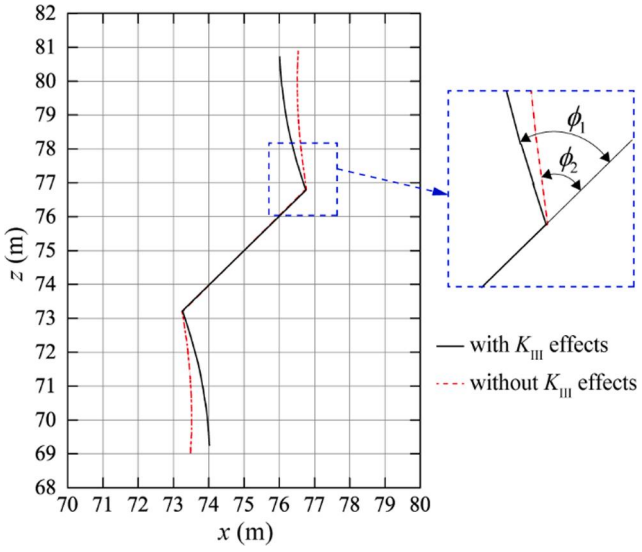

Fig. 34. Cross-section view (y = 75 m) of the fracture reorientation paths. The reorientation angles ϕ_1 and ϕ_2 are also shown.

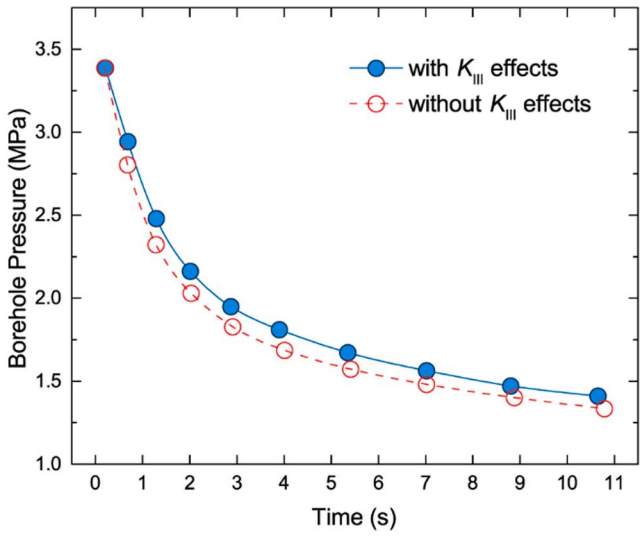

Fig. 35. Evolution of borehole pressure versus time with and without K_{III} effects.

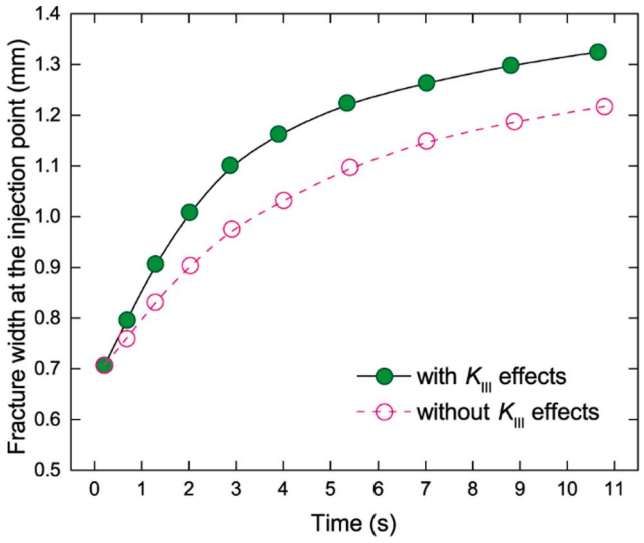

Fig. 36. Evolution of fracture width at the injection point versus time with and without K_{III} effects.

4.7. Growth of 8 penny-shaped fractures

This section is aimed to investigate the performance of the parallel implementation (Smith et al., 2014) of the proposed method using the Message Passing Interface (MPI). Thanks to the reduction technique and the element-by-element algorithm (Smith et al., 2014) where the assembly of global system matrices is avoided, the proposed method yields a high flexibility with respect to parallel implementation. In this study, an in-house mesh-partitioning tool called PhiPsi_MPT is adopted to perform the domain decomposition. After specifying DOFs numbers, sub-domains are allocated to processes. Model preparation, data reading and writing are implemented by using a single main process. In the meantime, equations are solved on processes and necessary communications between processes are carried out using MPI.

In this example, 8 initial parallel penny-shaped fractures of 1 m radius are vertically located at the center of a 100 × 100 × 160 m cubic domain, as shown in Fig. 37. The distance between any two adjacent fractures is 20 m. The injection rate of fluid of 0.1 Pa·s viscosity is 0.05 m^3/s for all fractures. All other parameters including in-situ stress,

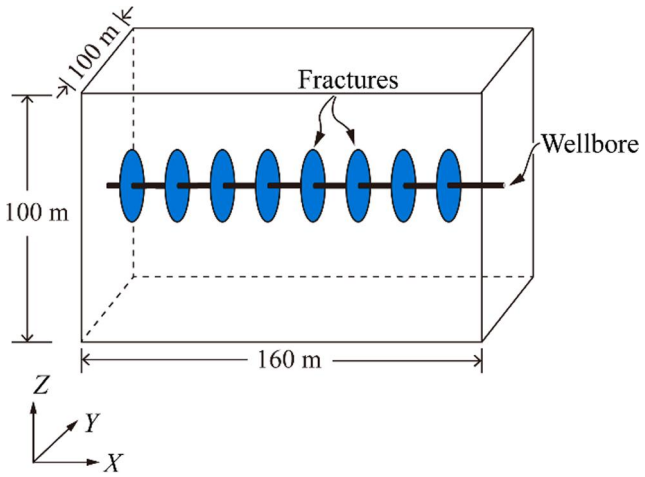

Fig. 37. Schematic of a cubic domain that contains 8 initial parallel penny-shaped fractures.

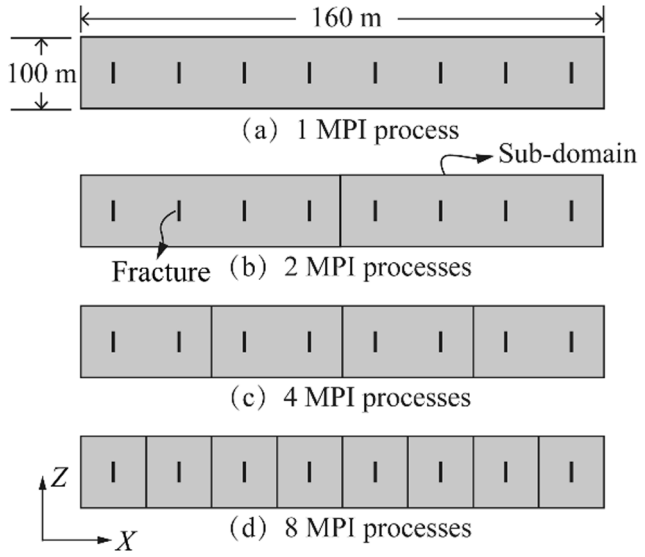

Fig. 38. Illustration of domain compositions shown in the *X-Z* plane for parallel computation using different numbers of MPI processes. The size of geometrical models in *z* direction is scaled in order to show all cases in one figure.

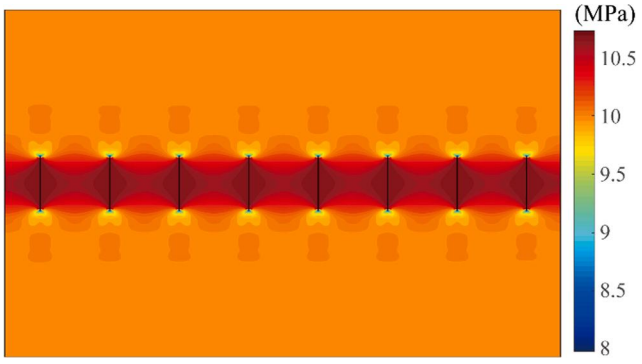

Fig. 39. Cross-section view ($y = 0$) of the stress distribution in × direction and the geometry of the propagated fractures. Positive values indicate compression stress.

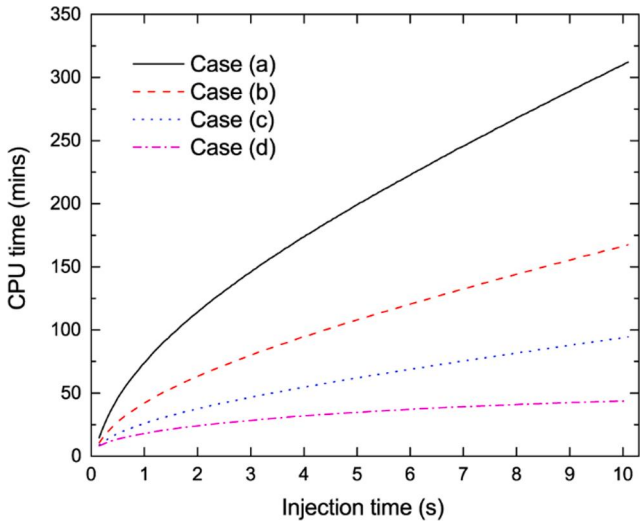

Fig. 40. Consumed CPU time versus injection time for cases (a) to (d).

Young's modulus, Poisson's ratio, and fracture toughness are the same as in Section 4.4. The mesh is locally refined with 0.25 × 0.25 × 0.25 m element within the region with a size of 10 × 10 × 5 m around each fracture. The total number of brick elements is 742,680. In this problem, instead of simulation results, we focus mainly on the CPU time of the simulation performed using different numbers of MPI processes. Four cases with different domain decomposition strategies are studied as illustrated in Fig. 38, numbers of fractures in each sub-domain for cases (a), (b), (c), and (d) are 8, 4, 2, and 1, respectively.

The cross-section view of the stress distribution in × direction is presented in Fig. 39. The stress shadow effect has not been observed due to the large spacing between fractures. The consumed CPU time versus injection time for cases (a) to (d) is shown in Fig. 40. Significant decreases of the total consumed CPU time can be observed. The speed-up (the ratio of the consumed CPU time required by the single process simulation to the consumed CPU time required by the multi-process simulation) for cases (b), (c), and (d) over case (a) is by a factor of 1.91, 3.69, and 7.03, respectively. These results illustrate very high effectiveness of parallel implementation of the proposed method. In fact, the proposed model can be readily implemented on massively parallel architectures.

5. Conclusions

In recent years, the XFEM has shown great flexibility and effectiveness in fracture propagation applications because of its mesh-independent feature. There is a considerable amount of XFEM-based literature on 2D hydraulic fracturing simulation in shale gas reservoirs, whereas, to the best of our knowledge, very little is available when it comes to 3D hydraulic fracturing problems. This paper shows how the XFEM can be efficiently used to simulate 3D non-planar fluid-driven fracturing applications in energy exploitation area. In order to do that, we present a fully-coupled approach in which an extended finite element method with high-order tip enrichment functions is used to simulate the rock deformation. Some challenging issues on the computational methodology, including the identification of fluid elements, the selection of enriched nodes and elements, and the subdivision of enriched elements are handled efficiently in virtue of the explicit description of the geometrical fractures. The discretized non-linear system of equations of the fully-coupled model is solved using the Newton-Raphson method in an element-by-element fashion in conjunction with the reduction technique through which only enriched DOFs are involved in the solution process. Besides, a displacement extrapolation method considering high-order terms is proposed to extract stress intensity factors from the displacement field.

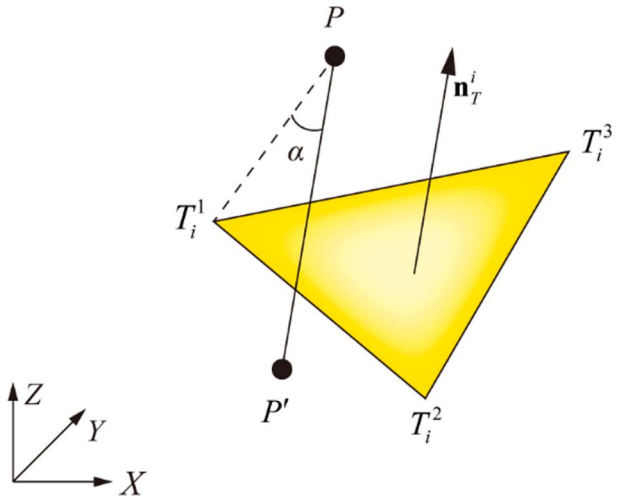

Fig. A1. The signed distance from a point P to triangle T_i.

Seven numerical examples are solved to illustrate the validity and performance of the proposed method. The first example shows that tip enrichment functions with high-order terms show better convergence rates and improved accuracy for both the L_2 norm and the energy norm of error. In addition, the proposed displacement extrapolation method with high-order terms can predict SIFs with higher accuracy. The fracture propagation model is validated in the second example by comparing with the analytical solution. Numerical solutions of both toughness-dominated and viscosity-dominated fracturing in the third example are in good agreement with analytical solutions, indicating the applicability and reliability of the fluid–solid coupling model. The propagation of two parallel penny-shaped fractures in the fourth example, where the stress shadow effect is well studied, illustrates that the reduction technique can significantly decrease the total CPU time by up to 53.5% without sacrificing the simulation accuracy. The validation of the proposed method against laboratory experimental data is presented in the fifth example, and good agreements are achieved. The effects of mode III loading on the fracture propagation path and the importance of K_{III} in a fracture propagation criterion are demonstrated in the sixth example. The performance of MPI parallel implementation of the proposed method is investigated in the last example with up to 742,680 hexahedral elements. The speed-up for the case with 8 MPI processes over the case with one process is by a factor of 7.03, indicating very high parallel performance of the proposed method.

The proposed method can be used as an easy-to-implement, flexible, and efficient numerical tool for modeling 3D non-planar fluid-driven fracture propagation in shale gas reservoirs or other application scenarios. In order to further improve the applicability of the proposed method, the permeability of rock formation and the fracture front segmentation will be considered in the following work. Other on-going work includes interactions between fluid-driven fractures and natural fractures, load balance algorithm for the parallel implementation with up to 1,000 processes, and large-scale engineering application tests. The present work is a first step that paves the road towards such simulations.

Declaration of Competing Interest

The authors declare that they have no known competing financial interests or personal relationships that could have appeared to influence the work reported in this paper.

Acknowledgements

This work was jointly supported by the National Natural Science

Foundation of China [51904111], the Natural Science Foundation of Jiangsu Province [BK20170457], and the Open Fund for Jiangsu Key Laboratory of Advanced Manufacturing Technology [HGAMTL-1712].

Appendix A. Signed distance from a point to a triangle patch

Let T_i^1, T_i^2 and T_i^3 be the triangle points of triangle T_i, and calculate the normal of T_i

$$\mathbf{n}_T^i = T_i^1T_i^2 \times T_i^1T_i^3 \tag{A.1}$$

Then, as illustrated in Fig. A1, the angle α between $\mathbf{n}_T^i$ and PT_i^1 can be obtained

$$\alpha = arccos\left(\frac{PT_i^1 \cdot \mathbf{n}_T^i}{|PT_i^1||\mathbf{n}_T^i|}\right) \tag{A.2}$$

The length of the vector from P to the foot of the perpendicular P' can be found using

$$|PP'| = |PT_i^1|cos\alpha \tag{A.3}$$

Finally, the signed distance from P to triangle T_i can be expressed as

$$d_{sign}^{T_i} = sign\left(det\begin{bmatrix} T_i^2 - T_i^1 \\ T_i^3 - T_i^1 \\ P - T_i^1 \end{bmatrix}\right)|PP'| \tag{A.4}$$

In order to check whether P' lies inside T_i, we introduce vectors $\mathbf{v}_0 = T_i^3 - T_i^1$, $\mathbf{v}_1 = T_i^2 - T_i^1$ and $\mathbf{v}_2 = \mathrm{P}' - T_i^1$. Two dimensionless parameters u and v are defined as

$$\begin{cases} u = \dfrac{(\mathbf{v}_1\cdot\mathbf{v}_1)(\mathbf{v}_2\cdot\mathbf{v}_0) - (\mathbf{v}_1\cdot\mathbf{v}_0)(\mathbf{v}_2\cdot\mathbf{v}_1)}{(\mathbf{v}_0\cdot\mathbf{v}_0)(\mathbf{v}_1\cdot\mathbf{v}_1) - (\mathbf{v}_0\cdot\mathbf{v}_1)(\mathbf{v}_1\cdot\mathbf{v}_0)} \\ v = \dfrac{(\mathbf{v}_0\cdot\mathbf{v}_0)(\mathbf{v}_2\cdot\mathbf{v}_1) - (\mathbf{v}_0\cdot\mathbf{v}_1)(\mathbf{v}_2\cdot\mathbf{v}_0)}{(\mathbf{v}_0\cdot\mathbf{v}_0)(\mathbf{v}_1\cdot\mathbf{v}_1) - (\mathbf{v}_0\cdot\mathbf{v}_1)(\mathbf{v}_1\cdot\mathbf{v}_0)} \end{cases} \tag{A.5}$$

Then, P' lies inside T_i if the following conditions can be satisfied

$$\begin{cases} u \geqslant 0 \\ v \geqslant 0 \\ u + v \leqslant 1 \end{cases} \tag{A.6}$$

Appendix B. Asymptotic solutions of the penny-shaped fluid-driven fracture

For a zero-toughness, penny-shaped fluid-driven fracture without leak-off, the asymptotic analytical solutions of the fracture radius R, the facture opening w and the net pressure p can be expressed as (Savitski and Detournay, 2002):

$$R(t) = 0.6955\left(\frac{Q_0^3E'}{\mu'}\right)^{\frac{1}{9}}t^{\frac{4}{9}} \tag{B.1}$$

$$w(\rho,t) = 0.6955[0.0705(13\rho + 21.0823)(1-\rho)^{\frac{2}{3}} + 0.236(\sqrt{1-\rho^2} - \rho\mathrm{arccos}\rho)](\frac{Q_0^3\mu'^2}{E'^2})^{\frac{1}{9}}t^{\frac{1}{9}} \tag{B.2}$$

$$p(\rho,t) = [0.8593 - \frac{0.2387}{(1-\rho)^{\frac{1}{3}}} - 0.09269\ln\rho](\mu'E'^2)^{\frac{1}{3}}t^{-\frac{1}{3}} \tag{B.3}$$

where $E' = E/(1-\nu^2)$, $\mu' = 12\mu$, $\rho = r/R$.

For a zero-viscosity fracture, the solutions can be written as follows (Savitski and Detournay, 2002):

$$R(t) = \mathscr{L}[0.8546 - 0.7349\mathscr{M}\mu'] \tag{B.4}$$

$$w(\rho,t) = \mathscr{E}\ominus\mathscr{L}\left\{0.6537\sqrt{1-\rho^2} + \mathscr{M}\left(0.8264 - 1.2397\left[\rho arccos\rho - 1.2\mathrm{I}^*(\rho) - 0.1069\sqrt{1-\rho^2}\right]\right)\right\} \tag{B.5}$$

$$p(\rho,t) = \mathscr{E}\ominus\mathrm{E}'\left\{0.3004 + \mathscr{M}\left[0.638 - 0.5697ln\rho + 0.3418ln\left(1-\rho^2\right)\right]\right\} \tag{B.6}$$

where $K' = 4\sqrt{2/\pi}K_{1c}$, $\mathscr{M} = \mu'(\frac{Q_0^3E'^{13}}{K'^{18}t^2})^{\frac{1}{5}}$, $\mathscr{E} = (\frac{K'^6}{E'^6Q_0t})^{\frac{1}{5}}$, $\mathscr{L} = (\frac{Q_0^2E'^2t^2}{K'^2})^{\frac{1}{5}}$, and

$$I^*(\rho) = \int_\rho^1 \sqrt{\frac{1-\xi^2}{\xi^2-\rho^2}} arcsin\xi d\xi \tag{B.7}$$

References

Abé, H., Keer, L.M., Mura, T., 1976. Growth rate of a penny-shaped crack in hydraulic fracturing of rocks. J. Geophys. Res. 81, 5335–5340.

Abelson, M., Agnon, A., 1997. Mechanics of oblique spreading and ridge segmentation. Earth Planet Sci Lett 148, 405–421.

Adachi, J., Siebrits, E., Peirce, A., Desroches, J., 2007. Computer simulation of hydraulic fractures. Int J Rock Mech Min Sci 44 (5), 739–757.

Agathos, K., Chatzi, E., Bordas, S.P.A., 2016. Stable 3D extended finite elements with higher order enrichment for accurate non planar fracture. Comput. Method Appl. M. 306, 19–46.

Bao, J.Q., Fathi, E., Ameri, S., 2014. A coupled finite element method for the numerical simulation of hydraulic fracturing with a condensation technique. Eng Fract Mech 131, 269–281.

Batchelor, G.K., 1967. An Introduction to Fluid Dynamics. Cambridge University Press, Cambridge.

Baydoun, M., Fries, T.P., 2012. Crack propagation criteria in three dimensions using the XFEM and an explicit-implicit crack description. Int. J. Fract. 178, 51–70.

Belytschko, T., Black, T., 1999. Elastic crack growth in finite elements with minimal remeshing. Int J Numer Methods Eng 45, 601–620.

Bordas, S., Moran, B., 2006. Enriched finite elements and level sets for damage tolerance assessment of complex structures. Eng Fract Mech 73, 1176–1201.

Bunger, A., Lecampion, B., Feng, X.-T., 2017. Rock Mechanics and Engineering. CRC Press, Boca Raton, Florida.

Cao, T.D., Hussain, F., Schrefler, B.A., 2018. Porous media fracturing dynamics: stepwise crack advancement and fluid pressure oscillations. J Mech Phys Solids 111, 113–133.

Dahi-Taleghani, A., Olson, J.E., 2011. Numerical modeling of multistranded-hydraulic-fracture propagation: Accounting for the interaction between induced and natural fractures. SPE J. 16 (3), 575–581.

Duflot, M., 2006. A meshless method with enriched weight funtions for three-dimensional crack propagation. Int. J. Numer. Methods Eng. 65, 1970–2006.

Duflot, M., 2007. A study of the representation of cracks with level sets. Int J Numer Methods Eng 70, 1261–1302.

Economides, M.J., Martin, T., 2007. Modern fracturing enhancing natural gas production. BJ Services Company, Houston, TX.

Feng, Y., Gray, K.E., 2017. Parameters controlling pressure and fracture behaviors in field injectivity tests: A numerical investigation using coupled flow and geomechanics model. Computers and Geotechnics. 87, 49–61.

Gordeliy, E., Peirce, A., 2013. Coupling schemes for modeling hydraulic fracture propagation using the XFEM. Comput Method Appl M. 253, 305–322.

Guinea, G.V., Planas, J., Elices, M., 2000. KI evaluation by the displacement extrapolation technique. Eng. Fract. Mech. 66, 243–255.

Guo, P., Cheng, Y., 2013. Permeability prediction in deep coal seam: a case study on the No. 3 coal seam of the Southern Qinshui Basin in China. The Scientific World Journal. 2013, 161457.

Gupta, P., Duarte, C.A., 2014. Simulation of non-planar three-dimensional hydraulic fracture propagation. Int J Numer Anal Methods Geomech 38, 1397–1430.

Gupta, P., Duarte, C.A., 2018. Coupled hydromechanical-fracture simulations of nonplanar three-dimensional hydraulic fracture propagation. Int J Numer Anal Methods Geomech 42, 143–180.

Gupta, P., Duarte, C.A., Dhankhar, A., 2017. Accuracy and robustness of stress intensity factor extraction methods for the generalized/eXtended Finite Element Method. Eng. Fract. Mech. 179, 120–153.

Haddad, M., Sepehrnoori, K., 2016. XFEM-bsed CZM for the simulation of 3D multiple-cluster hydraulic fracturing in quasi-brittle shale formations. Rock Mech Rock Eng 49, 4731–4748.

Hayashi, K., Sato, A., Ito, T., 1997. In situ stress measurements by hydraulic fracturing for a rock mass with many planes of weakness. Int J Rock Mech Min Sci 34, 45–58.

He, Q., Suorineni, F.T., Oh, J., 2016. Review of hydraulic fracturing for preconditioning in cave mining. Rock Mech Rock Eng 49, 4893–4910.

Huang, K., Zhang, Z., Ghassemi, A., 2013. Modeling three-dimensional hydraulic fracture propagation using virtual multidimensional internal bonds. Int. J. Numer. Anal. Methods Geomech. 37 (13), 2021–2038.

Jiménez, J.J., Segura, R.J., Feito, F.R., 2010. A robust segment/triangle intersection algorithm for interference tests. Efficiency study. Comput. Geometry: Theory Appl.. 43, 474–492.

Kanninen, M.F., Popelar, C.H., 1985. Advanced fracture mechanics. Oxford University Press, New York.

Ketterij, R.B.V., Pater, C.J.D., 1999. Impact of perforations on hydraulic fracture tortuosity. SPE Prod. Facilit. 14 (2), 117–130.

Klerk, J.G.F., 1969. A rapid method of predicting width and extent of hydraulically induced fractures. Journal of Petroleum Technology. 21, 1571–1581.

Klimenko, D., Taleghani, A.D., 2018. A modified extended finite element method for fluid-driven fractures incorporating variable primary energy loss mechanisms. Int J Rock Mech Min Sci 106, 329–341.

Kumar, D., Ghassemi, A., 2016. A three-dimensional analysis of simultaneous and sequential fracturing of horizontal wells. J Pet Sci Eng. 146, 1006–1025.

Kumari, W.G.P., Ranjith, P.G., Perera, M.S.A., Li, X., Li, L.H., 2018. Hydraulic fracturing under high temperature and pressure conditions with micro CT applications: Geothermal energy from hot dry rocks. Fuel. 230, 138–154.

Lan, M., Waisman, H., Harari, I., 2013. A direct analytical method to extract mixed-mode components of strain energy release rates from Irwin's integral using extended finite element method. Int J Numer Methods Eng 95, 1033–1052.

Lecampion, B., 2009. An extended finite element method for hydraulic fracture problems. Commun Numer Methods Eng 25 (2), 121–133.

Lecampion, B., Bunger, A., Zhang, X., 2018. Numerical methods for hydraulic fracture propagation: A review of recent trends. J Nat Gas Sci Eng. 49, 66–83.

Lhomme TP, Pater CJd, Helfferich PH. Experimental study of hydraulic fracture initiation in Colton sandstone. SPE/ISRM Rock Mechanics Conference. Irving, Texas: Society of Petroleum Engineers, 2002.

Loehnert, S., Mueller-Hoeppe, D.S., Wriggers, P., 2011. 3D corrected XFEM approach and extension to finite deformation theory. Int J Numer Methods Eng 86, 431–452.

Melenk, J.M., Babuška, I., 1996. The Partition of Unity Finite Element Method: Basic Theory and Applications. Eidgenossische Technische Hochschule. Switzerland, Seminar fur Angewandte Mathematik.

Meng YF, Luo PY, Jin L. Why low permeability and how does it affect coalbed methane supply in coal seams in China. SPE Eastern Regional Meeting. Columbus, Ohio: Society of Petroleum Engineers, 1996.

Milanese, E., Yılmaz, O., Molinari, J.-F., Schrefler, B., 2016. Avalanches in dry and saturated disordered media at fracture. Phys Rev E. 93, 043002.

Moës, N., Dolbow, J., Belytschko, T., 1999. A finite element method for crack growth without remeshing. Int J Numer Methods Eng 46 (1), 131–150.

Nordgren, R.P., 1972. Propagation of a vertical hydraulic fracture. SPE-3009-PA. 12, 306–314.

Okland D, Gabrielsen GK, Gjerde J, Koen S, Williams EL. The importance of extended leak-off test data for combatting lost circulation. SPE/ISRM Rock Mechanics Conference. Irving, Texas, 2002.

Papanastasiou, P., 1999. An efficient algorithm for propagating fluid-driven fractures. Comput Mech 24 (4), 258–267.

Paul, B., Faivre, M., Massin, P., Giot, R., Colombo, D., Golfier, F., et al., 2018. 3D coupled HM–XFEM modeling with cohesive zone model and applications to non planar hydraulic fracture propagation and multiple hydraulic fractures interference. Comput Method Appl M. 342, 321–353.

Pereira, J.P., Duarte, C.A., Jiao, X., 2010. Three-dimensional crack growth with hp-generalized finite element and face offsetting methods. Comput. Mech. 46, 431–453.

Perkins, T.K., Kern, L.R., 1961. Widths of hydraulic fractures. Journal of Petroleum Technology. 13, 937–949.

Peruzzo, C., Cao, D.T., Milanesec, E., Favia, P., Pesavento, F., Hussain, F., et al., 2019. Dynamics of fracturing saturated porous media and self-organization of rupture. European Journal of Mechanics. 74, 471–484.

Pizzocolo, F., Huyghe, J.M., Ito, K., 2013. Mode I crack propagation in hydrogels is step wise. Eng Fract Mech 97, 72–79.

Press, W.H., Teukolsky, S.A., Vetterling, W.T., Flannery, B.P., 1992. Numerical Recipes in Fortran: The Art of Scientic Computing. Cambridge University Press, New York.

Raziperchikolaee, S., Alvarado, V., Yin, S., 2013. Effect of hydraulic fracturing on long-term storage of CO2 in stimulated saline aquifers. Appl Energy 102, 1091–1104.

Rubin, A.M., 1995. Propagation of magma-filled cracks. Annual Review of Earth and Planetary Sciences. 23, 287–336.

Salimzadeh, S., Usui, T., Paluszny, A., Zimmerman, R.W., 2017. Finite element simulations of interactions between multiple hydraulic fractures in a poroelastic rock. Int. J. Rock Mech. Min. Sci. 99, 9–20.

Savitski, A.A., Detournay, E., 2002. Propagation of a penny-shaped fluid-driven fracture in an impermeable rock: asymptotic solutions. Int. J. Solids Struct. 39, 6311–6337.

Schöllmann, M., Richard, H.A., Kullmer, G., Fulland, M., 2002. A new criterion for the prediction of crack development in multiaxially loaded structures. Int. J. Fract. 117, 129–141.

Secchi, S., Schrefler, B.A., 2014. Hydraulic fracturing and its peculiarities. Asia Pacific Journal on Computational Engineering. 1, 8.

Shi, F., Wang, X., Liu, C., Liu, H., Wu, H., 2016. A coupled extended finite element approach for modeling hydraulic fracturing in consideration of proppant. J Nat Gas Sci Eng. 33, 885–897.

Shi, F., Wang, X., Liu, C., Liu, H., Wu, H., 2017. An XFEM-based method with reduction technique for modeling hydraulic fracture propagation in formations containing frictional natural fractures. Eng Fract Mech 173, 64–90.

Shimizu, H., Murata, S., Ishida, T., 2011. The distinct element analysis for hydraulic fracturing in hard rock considering fluid viscosity and particle size distribution. Int J Rock Mech Min Sci 48 (5), 712–727.

Shovkun, I., Espinoza, D.N., 2019. Propagation of toughness-dominated fluid-driven fractures in reactive porous media. Int J Rock Mech Min Sci 118, 42–51.

Smith IM, Griffiths DV, Margetts L. Programming the Finite Element Method. Fifth Edition ed. West Sussex, United Kingdom: John Wiley & Sons, 2014.

Sneddon, I.N., 1946;A-187:. The distribution of stress in the neighbourhood of a crack in an elastic solid. Proceedings of the Royal Society A. 229–260.

Song, G., Waisman, H., Lan, M., Harari, I., 2015. Extraction of stress intensity factors from Irwin's integral using high-order XFEM on triangular meshes. Int J Numer Methods Eng 102, 528–550.

Sukumar, N., Moës, N., Moran, B., Belytschko, T., 2000. Extended finite element method for three-dimensional crack modelling. Int J Numer Methods Eng 48, 1549–1570.

Tang, H., Wang, S., Zhang, R., Li, S., Zhang, L., Wu, Y., 2019. Analysis of stress interference among multiple hydraulic fractures using a fully three-dimensional displacement discontinuity method. J Pet Sci Eng. 179, 378–393.

Trimonova M, Baryshnikov N, Zenchenko E, Zenchenko P, Turuntaev S. The study of the unstable fracure propagation in the injection well: numerical and laboratory modeling. SPE Russian Petroleum Technology Conference. Moscow, Russia, 2017.

Wang, H.Y., 2016. Numerical investigation of fracture spacing and sequencing effects on multiple hydraulic fracture interference and coalescence in brittle and ductile reservoir rocks. Eng Fract Mech 157, 107–124.

Williams, M.L., 1957. On the stress distribution at the base of a stationary crack. J Appl Mech Tech Phys 24, 109–114.

Wu, R., Bunger, A.P., Jeffrey, R.G., Siebrits, E., 2008. A comparison of numerical and experimental results of hydraulic fracture growth into a zone of lower confining stress. The 42nd US Rock Mechanics Symposium (USRMS). San Francisco, California: American Rock Mechanics Association.

Wu, R., Germanovich, L.N., Hurt, R.S., 2009. Experimental and theoretical study of mixed-mode I+III crack propagation and segmentation. American Rock Mechanics Association, Asheville, North Carolina.